Variable Speed of Light Cosmology and Electromagnetism

Santosh Devasia

© May 2022, Santosh Devasia
All Rights Reserved

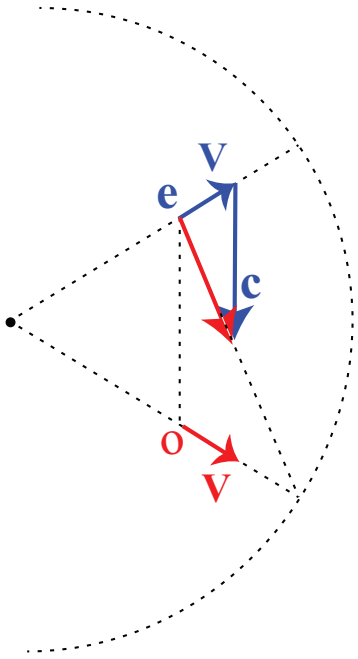

Contents

Abstract

This work explores modifications of electromagnetism models to allow variable speed of light (VSL) without violating current observations and investigates the utility of VSL to explain anomalies (unexplainable observations) in cosmology. Such a variable speed of light (VSL) approach, where the source speed augments the speed of light, is controversial since it violates Maxwell's equations that requires the speed of light to be independent of the source speed. Therefore, relative-velocity (RV) based modifications of Maxwell's equations are proposed to facilitate a VSL-based cosmology, that predicts (rather than assume) the Hubble law and explains current cosmological anomalies such as the apparent lack of time dilation in quasar observations. It is shown also that the proposed RV-based model matches current observations in electromagnetism and optics, such as the transverse Doppler effect and the Fresnel drag. Finally, a method to potentially validate/refute the proposed approach using high-speed ion experiments is proposed. [1] [2] [3]

[1] Chapter 1 is an adapted version reprinted by permission of Physics Essays Publication, from "Santosh Devasia, *Ritz-type Variable Speed of Light (VSL) Cosmology*, Physics Essays, Vol. 27 (4), pp. 523-536, December 2014."

[2] Chapter 2 is an adapted version reprinted from "S. Devasia, *Nonlinear Models for Relativity Effects in Electromagnetism*, Zeitschrift fur Naturforschung A, Vol. 64a (5-6), pp. 327-340, May-June, 2009."

[3] Chapter 3 is an adapted version reprinted with kind permission of The European Physical Journal (EPJ), from "S. Devasia, *Lorentz Violation in High-Energy Ions*, The European Physical Journal C, Vol. 69 (3-4), pp. 343-346, October 2010"
and "S. Devasia (2017). Reply to comment on: Lorentz violation in high-energy ions. ResearchWorks Archive. https://doi.org/10.6069/PDCN-Z183" "

1 Relative-velocity-based cosmology

1.1 Overview

The large number of anomalies in cosmological observations has led to substantial interest in alternatives to the standard big-bang type cosmology, e.g., [1–5]. These anomalies, which are challenging to explain using current models, include the large number of observed spectroscopic binaries with short time periods even though nearby visual binaries are not seen with such short time periods. Another anomaly is the apparent lack of time dilation in quasar observations [6] even though time dilation has been observed in supernovae (SNe) light curves [7] Some quasars also appear be closer than the distance indicated by their spectroscopic redshifts due to potential links with low redshift galaxies [8] as well as the presence of high-speed ejecta [9]. Finally, in SNe observations, challenges arise in explaining the farther-dimmer effect [10] as well as in identifying SNe progenitors [11]. These challenges make cosmology an important arena for testing the potential and the limitations of new theories in physics.

This chapter develops a variable-speed-of-light (VSL) cosmology model. The proposed model predicts the Hubble law and time dilation seen in current cosmological observations [7] as shown in Section 1.3. Periodic photosphere motions are investigated for its effect on VSL cosmology and its ability to match stellar observations in Section 1.4. Issues in quasar observations such as the apparent lack of time dilation in quasar light curves [6] even though time dilation has been observed in supernovae (SNe) light curves [7] are studied in Section 1.5. The model is used to also investigate, in Section 1.5, observations that (i) link some quasars with low redshift galaxies [8, 9]; and (ii) indicate the presence of superluminal ejecta [12]. Consistency of the model with recent farther dimmer relation [10] in supernovae (SNe) observations is shown in Section 1.6. The proposed model leads to temporal-and-spatial distortions in cosmological observations — the impact of such distortions is discussed in Section 1.7. Finally, potential large-scale anisotropies, e.g., in the Hubble constant, are discussed in Section 1.8, which is followed by the chapter conclusions.

1.2 Main Axioms

The main contribution of this chapter is to propose a Ritz-type, variable-speed-of-light (VSL) cosmology model based on the following two axioms.

1. [Velocity Axiom] Velocity of the source augments the speed of light [13, 14].
2. [Geometry Axiom] The cosmos is contained in a spherical shell that is expanding at a constant speed V.

The first axiom, wherein the velocity of the source augments the speed of light, is controversial. It is noted that VSL has been used, previously, in cosmology models [15], where physical constants (such as the gravitational constant) are allowed to vary over time. The relationships between the temporal variations of the different physical constants can be determined to match physical observations such as relativistic electromagnetism. The current article evaluates the potential for an alternate (Ritz-type VSL) model to match cosmological observations and explain current anomalies. Several researchers had suggested investigating astronomical data to test such VSL models – such astronomical observations (e.g., irregularities in observations of double-star system) that were initially thought to be contradictory were later found to be consistent [13]. Nevertheless, there remained several challenges such as the inability to (i) explain Fresnel drag and (ii) the lack of an accompanying electromagnetic theory, which would require modification of Maxwell's equations. These issues were recently reconsidered in [16], which seeks to extend Maxwell's equations for enabling a Ritz-type VSL, and is described further in Chapter 2. Methods to assess the proposed theory are discussed in Chapter 3.

The second axiom allows the kinetic energy to remain constant in a big-bang-type model without the need to have a size-dependent velocity as in Newtonian cosmology [17]. The second axiom could be modified to allow for potential reduction in the expansion speed V over time as the cosmos accumulates additional mass, or a potential increase in speed V due to the addition of a cosmological force. However, these are not considered in this article.

1.3 Consistency with Hubble Law

The proposed model can be used to derive the Hubble law (as opposed to being an empirical observation in current cosmology) as shown below.

1.3.1 The model

Consider a big-bang-type model where the universe (containing astrophysical objects) is a uniformly expanding spherical shell (geometry axiom), which is similar to Newtonian cosmology models, e.g., [17]. However, in contrast to the Newtonian cosmology model where the expansion speed increases linearly with the distance from the center [17], the expansion speed is constant in the current model. Nevertheless, it is shown that even with a constant expansion speed, the Ritz-type VSL model is consistent the farther-dimmer relation seen in recent SNe-based observations [10].

Consider light emitted in all directions at the standard speed of light c and frequency ν_e by an emitter e when it is at the location e_e at time t_1 as shown in Fig. 1.1. According to the geometry axiom, the emitter is moving at constant speed V, i.e., velocity $V_e\ \underline{r}_e = V\ \underline{r}_e$ with respect to an inertial frame I_a at a central position a as shown in Fig. 1.1, where $\underline{r}_e$ is a fixed, unit vector.

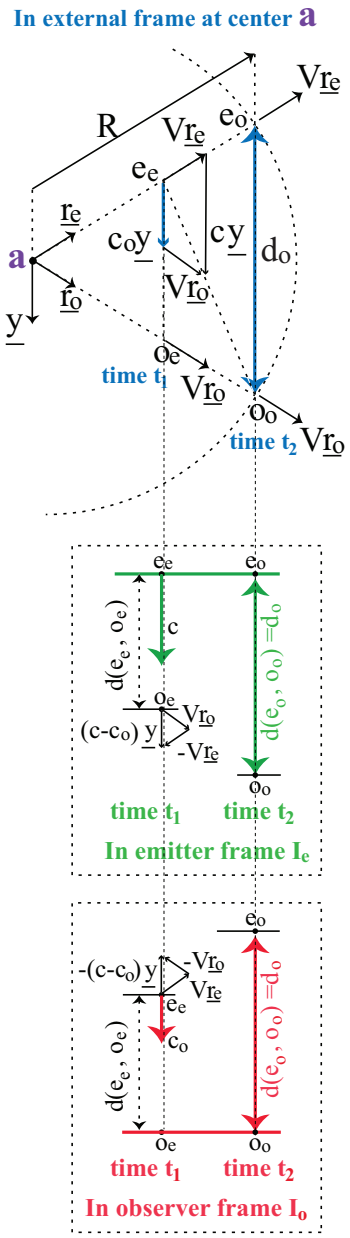

Figure 1.1: *VSL based on reference frames: (top) reference frame at center a of cosmological shell; (middle) reference frame associated with the emitter; (bottom) reference frame associated with the observer. Light emitted from point e_e at time t_1 reaches observer at o at time t_2, after time $\Delta t_{1,2} = t_2 - t_1$. Distances at observation time t_2 of the emitter and observer from the center are $d(ae_o) = R$ and $d(ao_o) = R$, respectively. Both emitter and observer are moving away from the center a at constant velocity (V_e and V_o) of magnitude V. Distance between observer and emitter at emission time t_1 is $d(e_e, o_e) = d_e$ and at observation time t_2 is $d(e_o, o_o) = d_o$.*

After time $\Delta t_{1,2}$, the light reaches an observer o at location o_o at time $t_2 = t_1 + \Delta t_{1,2}$, where the observer is moving at constant velocity

$$V_o \, \underline{r}_o \; = \; V \, \underline{r}_o \tag{1.1}$$

with respect to the inertial frame I_a and $\underline{r}_o$ is a fixed, unit vector. With respect to the emitter inertial frame I_e (moving with the emitter as shown in Fig. 1.1), during the time interval $\Delta t_{1,2}$, light has traveled a distance

$$d_o \quad = d(e_o, o_o) \quad = c\Delta t_{1,2}, \tag{1.2}$$

i.e., reached a shell of radius d_o centered at e_o at time t_2.

The speed c_o of the light observed in an inertial frame I_o on the observer o (at location o_o) is given by

$$c_o \underline{y} = V_e \underline{r}_e \; + c\underline{y} - V_o \underline{r}_o \; = \; V \underline{r}_e \; + c\underline{y} - V \underline{r}_o \tag{1.3}$$

where $\underline{y}$ is a fixed unit vector. As in Ritz-type models, the velocity of light $\underline{c}$ is added to the velocity of the source $\underline{v}_s$, i.e., $\underline{c} + \underline{v}_s$ to find the propagation velocity (the velocity axiom) in the relative-velocity-based approach. Although the proposed approach is different from the tired-light-type hypothesis, e.g., [1], the current model also results in a distance-redshift relation that matches the Hubble law as shown below.

The magnitude c_o of the observed light velocity can be found using the similar triangles $\triangle(ae_eo_e)$ and $\triangle(ae_oo_o)$, to obtain the following relationship between: (i) R the distance $d(ae_o) = d(ao_o)$; and (ii) $d_e \; = d(e_e, o_e)$ the distance between observer and emitter at the emission time instant t_1

$$\frac{d_e}{d_o} \; = \; \frac{c_o \Delta t_{1,2}}{c \Delta t_{1,2}} \; = \; \frac{c_o}{c} \; = \; \frac{R - V\Delta t_{1,2}}{R} \; = \; \frac{R - V(d_o/c)}{R} \; = \; 1 - \frac{V}{Rc} d_o. \tag{1.4}$$

Moreover, since $(R - V\Delta t_{1,2}) \leq R$, the observed light speed c_o is less than the standard speed of light c from Eq. (1.4), i.e.,

$$c_o \leq c. \tag{1.5}$$

1.3.2 Time dilation and red shift

The cosmological expansion and the reduction in observed light speed lead to three effects discussed below: (i) perceived time dilation; (ii) redshift; and (iii) energy reduction.

Perceived time dilation:

The emitter is seen to move away from the observer (in the observer frame of reference I_o) at a speed $V_{e,o}$ described by (from Eq. 1.3)

$$V_{e,o} \underline{y} \; = V \underline{r}_e - V \underline{r}_o \; = [c - c_o] \, \underline{y}. \tag{1.6}$$

Consider two photons emitted at time instants t_1 and $t_1 + t_e$ (in the emitter frame I_e), which move towards the observer at speed c_o. During the time interval t_e, the distance

$d_e = d(e_e, o_e)$ between the emitter and the observer has increased by $V_{e,o}t_e$. Hence the time interval t_o between the observation of the photons (in the observer frame I_o) is given by (from Eq. 1.6)

$$t_o \;=\; \left[t_e + \frac{d_e + V_{e,o}t_e}{c_o}\right] - \frac{d_e}{c_o} \;=\; \left[t_e + \frac{(c - c_o)t_e}{c_o}\right] \;=\; \frac{c}{c_o}t_e. \tag{1.7}$$

Therefore, a time interval t_e in the emitter frame appears (optically) as a dilated time interval t_o in the observer frame with

$$t_o \;= (c/c_o)t_e \;\geq t_e. \tag{1.8}$$

since $c \geq c_o$ by Eq. (1.5). Consequently, events in the emitter frame I_e appear (optically) to occur at a slower rate in the observer frame I_o, leading to a perceived time dilation.

Redshift:

The observed frequency ν_o is reduced with respect to the emitted frequency ν_e due to the Doppler effect. For example, $N_\nu = \nu_e t_e$ pulses sent at frequency ν_e in time t_e from the emitter is received at the observer in time t_o (as in Eq. 1.8). Therefore, the observed frequency ν_o is (by using Eq. 1.8)

$$\nu_o \;= \frac{N_\nu}{t_e} \;= \frac{t_e}{t_o}\nu_e \;= \frac{c_o}{c}\nu_e, \tag{1.9}$$

which corresponds to a redshift $z \geq 0$ given by

$$z \;= \frac{\nu_e - \nu_o}{\nu_o} \;= \frac{\nu_e}{\nu_o} - 1 \;= \frac{c}{c_o} - 1 \tag{1.10}$$

that can be rewritten as

$$1 + z \;= \frac{c}{c_o}. \tag{1.11}$$

Moreover, the distance d_o in Eq. (1.4) can be rewritten in terms of the redshift z as

$$d_o \;=\; \frac{Rc}{V}\left[1 - c_o/c\right] \;=\; \frac{Rc}{V}\left[1 - \frac{1}{1+z}\right] \;=\; \frac{Rc}{V}\left[\frac{z}{1+z}\right] \tag{1.12}$$

and the observed frequency in Eq. (1.9) can be rewritten as

$$\nu_o \;= \frac{c_o}{c}\nu_e \;= \frac{1}{1+z}\nu_e. \tag{1.13}$$

Note that the time dilation can be written in terms of the red shift as (from Eqs. 1.8, 1.11)

$$t_o \;= (c/c_o)t_e \;= (1+z)t_e. \tag{1.14}$$

Energy reduction:

The energy of a photon is reduced in the observer inertial frame I_o when compared to the emitter inertial frame I_e due to the reduction in the photon frequency between the two frames, from ν_e to ν_o given by Eq. (1.13). The ratio of perceived energy E_o (of photons) in the observer frame to the energy E_e (of the corresponding photons) in the emitter frame is given by

$$\frac{E_o}{E_e} = \frac{h\nu_o}{h\nu_e} = \frac{1}{(1+z)} \tag{1.15}$$

where h is the Planck constant.

Remark 1 *The time dilation of $1+z$ is consistent with cosmological observations such as the time broadening of supernovae (SNe) light curves [7].*

Remark 2 *In addition to the change in the observed energy of the light-quanta due to a reduction of the observed frequency (as in Eq. 1.15), the observed energy is reduced by time dilation (as in Eq. 1.14) since it leads to a change in the arrival rate of light-quanta. Both these effects were suggested as corrections by Hubble [18].*

1.3.3 Luminosity distance and red shift

Let L_e be the total energy of photons emitted from e_o per unit time. Then, the energy $L_e\Delta t_e$ emitted in a small time interval Δt_e is spread over a shell of radius d_o centered at point e_o after time t as in Fig. 1.1. The resulting energy per unit surface area E_e of this shell (in the emitter inertial frame I_e) is given by, from Eq. (1.12),

$$E_e = \frac{L_e}{4\pi d_o^2}\Delta t_e = \frac{L_e}{4\pi(\frac{Rc}{V})^2(\frac{z}{1+z})^2}\Delta t_e \tag{1.16}$$

In particular, the energy per unit surface area E_o observed at o_2 in the dilated-time interval Δt_o (in the observer inertial frame I_o) is, from Eqs. (1.14-1.16)

$$E_o = \frac{L_e}{4\pi(\frac{Rc}{V})^2(\frac{z^2}{(1+z)})}\frac{\Delta t_o}{(1+z)} = \frac{L_e\Delta t_o}{4\pi[(Rc/V)z]^2} = \frac{L_e\Delta t_o}{4\pi[d_L]^2}. \tag{1.17}$$

Then, the observed brightness B_o (i.e., energy per unit area per unit time in the observer inertial frame I_o at o_o) is given by

$$B_o = E_o/\Delta t_o = \frac{L_e}{4\pi[(Rc/V)z]^2} = \frac{L_e}{4\pi[d_L]^2} \tag{1.18}$$

Finally, the observed luminosity distance d_L increases linearly with the redshift z as

$$d_L = \frac{Rc}{V}z = (H)^{-1}cz, \tag{1.19}$$

which can be re-written as (the Hubble law)

$$V_{apparent} \quad = cz \quad = H\ d_L \tag{1.20}$$

where $V_{apparent}$ is the apparent speed away from the observer (based on the redshift z) and

$$H = V/R \tag{1.21}$$

is the Hubble constant.

Remark 3 (Variation in Hubble constant) *The model results in the prediction of observed redshift with distance. Over time t, the perceived instantaneous Hubble constant $H(t) = V/R(t)$ can decrease as the radius $R(t)$ of the cosmos increases. The rate of decrease is negligible if the expansion speed V is small compared to the radius $R(t)$.*

1.3.4 Relation between the different distances

The model yields the expected relation between the angular distance d_e, the proper distance d_o, and the observed luminosity distance d_L, as described below. In the observer inertial frame I_o, the emission is initiated at distance d_e — although the emitter is then seen to move away at speed $c - c_o$. Therefore, the angle θ_e of the emitter in the sky and the perceived size S_e are related to the angular distance d_e as $S_e = \theta_e d_e$. The distance d_o between the emitter and observer at the observation time is considered as the proper distance at the time of observation. The luminosity distance d_L and the proper distance d_o are related as (from Eqs. 1.12, 1.19)

$$d_o = \frac{Rc}{V} z \left[\frac{1}{1+z}\right] \quad = \quad \frac{d_L}{1+z}. \tag{1.22}$$

Moreover, the angular distance d_e and the proper distance d_o are related as (from Eqs. 1.4, 1.11)

$$d_e \quad = \quad \frac{c_o}{c} d_o \quad = \quad \frac{d_o}{1+z}, \tag{1.23}$$

resulting in the following relation between the luminosity distance d_L, the proper distance d_o, and the angular distance d_e

$$d_L \quad = \quad (1+z) d_o \quad = \quad (1+z)^2 d_e. \tag{1.24}$$

Remark 4 (Matching distance relationships) *The relationship between the angular distance d_e, the proper distance d_o, and the observed luminosity distance d_L in Eq. (1.24) is a direct result of the model's axioms, and matches observed relationship to the redshift z.*

1.4 Effect of VSL on Stellar Observations

The observed time dilation is affected by the speed and radius of the photosphere; the associated distortion of the light curves from nearby stars is studied in this section.

1.4.1 Periodic photosphere motion

Consider a nearby star at distance $d_{e,o}$, for which cosmological expansion effects (such as time dilation) are negligible. This allows the following analysis to focus on just the effect of the velocity addition on the speed of light. Let the motion of the photosphere be periodic, and consider one time period, i.e., time interval $[t_{ei}, t_{ei}+T_p]$ where T_p is time period of the photosphere motion. For any time instant $t = t_{ei}+t_e \in [t_{ei}, t_{ei}+T_p]$, i.e., for the shifted, emission time $t_e = (t - t_{e.i}) \in [0, T_p]$, let the acceleration $a_p(t_e) = c\dot{\beta}_p(t_e)$ of the photosphere be given by

$$\dot{\beta}_p(t_e) = f_p(t_e) + C_a \tag{1.25}$$

where $f_p(t_e)$ is a periodic function with time period T_p in the emitter frame I_p. Note that the functions are described in terms of the shifted, emission time t_e. The constant C_a is chosen such that the speed $v_p = c\beta_p$ of the photosphere is periodic (with time period T_p) and continuous at the endpoints of the time interval $t_e \in [0, T_p]$, e.g.,

$$\begin{aligned} \frac{v_p}{c}(T_p) - \frac{v_p}{c}(0) &= \beta_p(T_p) - \beta_p(0) = \int_0^{T_p} \dot{\beta}_p(t_e)dt_e \\ &= T_p C_a + \int_0^{T_p} f_p(t_e)dt_e = 0. \end{aligned} \tag{1.26}$$

Moreover, the constant $v_p(0)$ is chosen to ensure that the radial photosphere position $r_p(t_e)$ of the photosphere is periodic and continuous at the endpoints of the time interval $t_e \in [0, T_p]$, e.g.,

$$\frac{r_p}{c}(T_p) - \frac{r_p}{c}(0) = \int_0^{T_p} \beta_p(t_e)dt_e = 0. \tag{1.27}$$

An example photosphere trajectory is shown in Fig. 1.2.

1.4.2 Observation and emission time intervals

Consider two photons emitted at shifted time instants t_{ei} and $t_{ei}+t_e$. The emitted photons move towards the observer at speeds $c + c\beta_p(0)$ and $c + c\beta_p(t_e)$ in the emitter frame I_e. Let the photons reach an observer o (at a distance $d_{e,o}$) at time instants t_{oi} and $t_{oi}+t_o$, respectively, where

$$t_{oi} = t_{ei} + \frac{d_{e,o} - r_p(0)}{c + c\beta_p(0)} \tag{1.28}$$

$$t_{oi} + t_o = t_{ei} + t_e + \frac{d_{e,o} - r_p(t_e)}{c + c\beta_p(t_e)}, \tag{1.29}$$

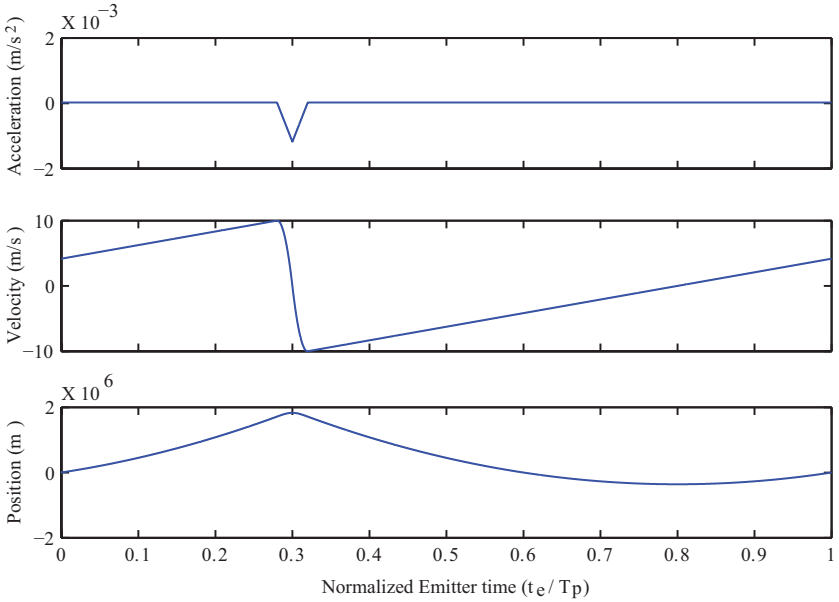

Figure 1.2: *Example periodic photosphere motion. The acceleration varies linearly in the time intervals* $t_e/T_p \in [0.28, 0.3]$, $t_e/T_p \in [0.3, 0.32]$ *and is constant elsewhere. Specific values of the acceleration are* $a_p = 2.4 \times 10^{-5} m/s^2$ *at* $t_e/T_p = 0$ *and* $a_p = -1.2 \times 10^{-3} m/s^2$ *at* $t_e/T_p = 0.3$

and t_o is the shifted, observation time, which can be found by subtracting the two expressions in Eq. (1.29), leading to

$$\begin{aligned} t_o &= t_e + \frac{d_{e,o}}{c}\left[\frac{1}{1+\beta_p(t_e)} - \frac{1}{1+\beta_p(0)}\right] - \left[\frac{\frac{r_p(t_e)}{c}}{1+\beta_p(t_e)} - \frac{\frac{r_p(0)}{c}}{1+\beta_p(0)}\right] \\ &= t_e - \frac{d_{e,o}}{c}\frac{\beta_p(t_e)-\beta_p(0)}{[1+\beta_p(t_e)][1+\beta_p(0)]} - \left[\frac{\frac{r_p(t_e)}{c}}{1+\beta_p(t_e)} - \frac{\frac{r_p(0)}{c}}{1+\beta_p(0)}\right] \end{aligned} \tag{1.30}$$

For periodic emissions (with period T_p in the emitter reference frame), with small photosphere speeds ($\beta_p << 1$), and relatively small variation in radius (r_p) , the second term can be neglected and the above Eq. (1.30) can be simplified to

$$\begin{aligned} t_o &\approx t_e - T_p\left[\beta_{p,max}\frac{d_{e,o}/c}{T_p}\right]\frac{\beta_p(t_e)-\beta_p(0)}{\beta_{p,max}} \\ &= t_e - T_p\left[\Gamma_p\right]\frac{\beta_p(t_e)-\beta_p(0)}{\beta_{p,max}} \end{aligned} \tag{1.31}$$

where $c\beta_{p,max}$ corresponds the the maximum magnitude of the photosphere speed. Without photosphere motion, the shifted, observation and emission times would be equal, i.e., $t_o = t_e$. However, for the same emission time interval t_e, the observation time interval t_o can be smaller if the photosphere speed β_p is larger since it takes less time for the emission to travel the distance $d_{e,o}$ at speed $c(1+\beta_p)$.

The observation and emission time intervals t_o, t_e (as in Eq. 1.31) are compared in Fig. 1.3 for the photosphere motion in Fig. 1.2. The parameter Γ_p in in Eq. (1.31), is chosen to be $\Gamma_p = 4 \times 10^{-4}$, which corresponds to time period T_p of 10 days; distance d of 100 parsecs; and maximum (absolute) value of photosphere speed $v_p = 10$ m/s. Note that other combinations of these terms can also lead to the same value of parameter Γ_p. The observation and emission time intervals t_o, t_e are similar; for clarity, one of the curves (t_o/T_p) is displaced upwards in the top plot of Fig. 1.3. Moreover, the difference $(t_o - t_e)/T_p$ is shown in the bottom plot in Fig. 1.3. Note that the difference between the observation and emission time intervals $(t_o - t_e)/T_p$ (in Fig. 1.3) has an inverse relationship to the photosphere speed in Fig. 1.2.

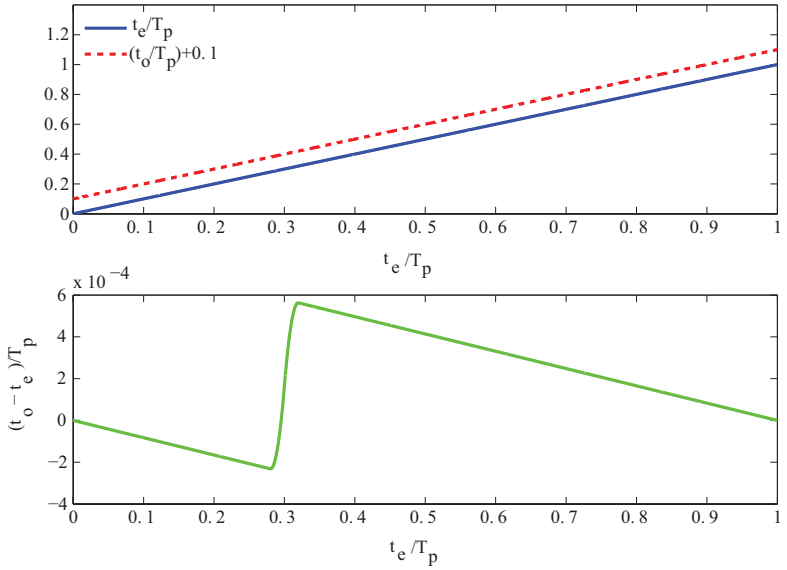

Figure 1.3: *Comparison of normalized (and shifted) observation time t_o/T_p (as in Eq. 1.31 with $\Gamma_p = 4 \times 10^{-4}$) and normalized (and shifted) emission time t_e/T_p for the photosphere motion in Fig. 1.2.*

1.4.3 Brightness variation follows photosphere acceleration

If the energy-emission rate from the star is constant, then without photosphere motion, the observed brightness (B_o) is uniform, i.e., $B_o(t_o) = B^*$. However, with photosphere motion, photons that are emitted in evenly spaced intervals are not observed in evenly spaced intervals due to changes in the time t_o between observations as quantified in Eq. (1.31). The variation in the observed brightness (due to the difference between the observation and emission time intervals) is numerically evaluated by discretizing the emission times into small intervals, and mapping the emitted photons into discretized observation time intervals. The resulting observed brightness B_o, with and without photosphere motion, is compared shown in Fig. 1.4.

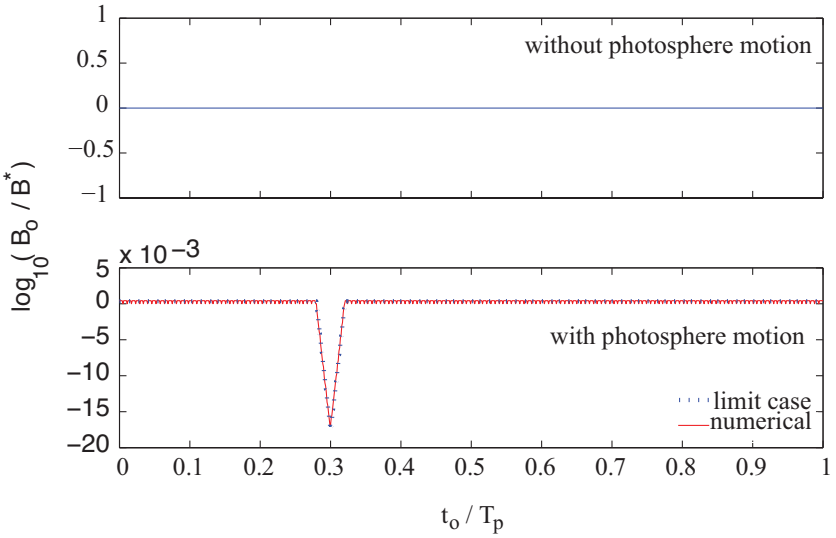

Figure 1.4: *Comparison of observed brightness without (top) and with (bottom) photosphere motion (using Eq. 1.31). The observed brightness B_o has a similar trend as the photosphere acceleration a_p (in Fig. 1.2) even though the energy-emission rate is uniform.*

With a small photosphere motion, the variation of the observed brightness (in Fig. 1.4) has a similar trend as the photosphere acceleration a_p (in Fig. 1.2), even without variations in the rate of energy emission. To clarify this, photons observed during a small time interval Δt_o around the observation time t_o can be related to those from the associated emission time interval Δt_e as (from Eq. 1.31)

$$\begin{aligned}\Delta t_o &= \left[\frac{dt_o}{dt_e}(t_e)\right]\Delta t_e = \left[1-\left(\frac{\Gamma_p T_p}{\beta_{p,max}}\right)\frac{d\beta_p}{dt_e}(t_e)\right]\Delta t_e \\ &= \left[1-\left(\frac{\Gamma_p T_p}{c\beta_{p,max}}\right)a_p(t_e)\right]\Delta t_e = \left[1-\left(\frac{d_{e,o}}{c^2}\right)a_p(t_e)\right]\Delta t_e. \end{aligned} \tag{1.32}$$

Hence, the observed brightness, with photosphere motion, is related to the brightness B^* without photosphere motion by

$$B_o(t_o) = B_o^*\frac{\Delta t_e}{\Delta t_o} = B_o^*\frac{1}{1-\left(\frac{d_{e,o}}{c^2}\right)a_p(t_e)}, \tag{1.33}$$

where the observation and emission time intervals (t_o, t_e) are related by Eq. (1.31). In the logarithmic scale, for sufficiently small photosphere motions, i.e., sufficiently small acceleration a_p,

$$\begin{aligned}\log_{10}\left[B_o(t_o)\right] &= \log_{10} B^* - \log_{10}\left[1-\left(\frac{d_{e,o}}{c^2}\right)a_p(t_e)\right] \\ &\approx \log_{10} B^* + \left[\frac{1}{ln(10)}\left(\frac{d_{e,o}}{c^2}\right)\right]a_p(t_e)\end{aligned} \tag{1.34}$$

which results in

$$\log_{10}\left[\frac{B_o(t_o)}{B^*}\right] = [\alpha_B]\, a_p(t_e). \tag{1.35}$$

Thus, the variation in the observed brightness $\log_{10}[B_o(t_o)]$ (light curve) reflects the photosphere acceleration when the photosphere motion is small and slowly varying. This similarity in the observed light curves is seen in Fig. 1.4, which compares the numerically computed brightness (for the example photosphere motion) and the limit case (in Eq. 1.35) for small, sufficiently-slowly-varying, photosphere motions.

The difference between the observation and emission time intervals (t_o, t_e) increases with the parameter Γ_p in Eq. (1.31). Hence, the brightness variation can change substantially from the limit case (in Eq. 1.35). To illustrate, the parameter Γ_p is increased from 4×10^{-4} to 4 and the resulting brightness variation (light curves) over a time period is shown in Fig. 1.5, which has similar patterns to typical light curves of binary star observations.

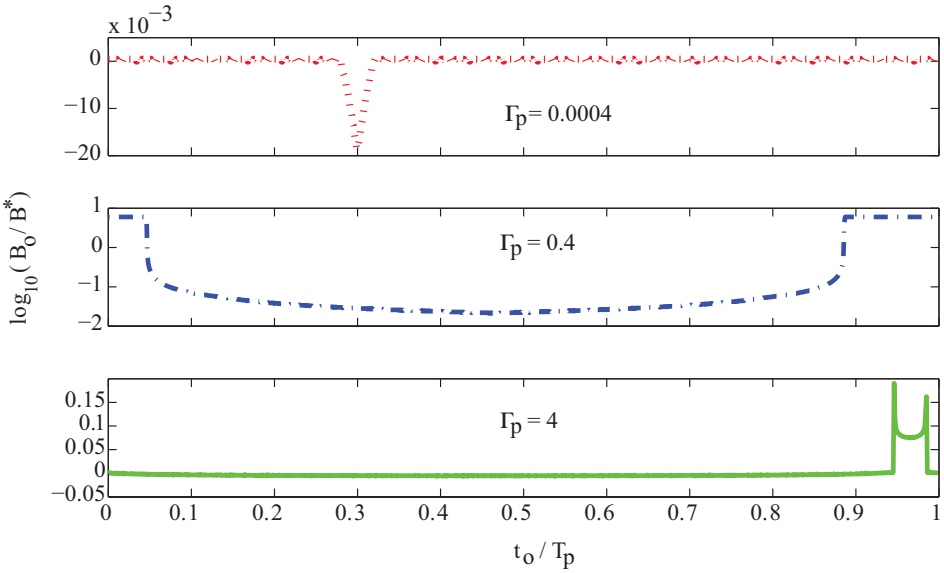

Figure 1.5: *Observed light curves for different values of the parameter Γ_p in Eq. (1.31).*

Remark 5 *Other types of photosphere acceleration (e.g., sinusoidal) are possible. The possible set of acceleration time patterns depends on the type of photosphere vibrations and the stellar dynamics.*

1.4.4 Photosphere vibration and apparent binaries

Different regions of the photosphere vibrations can have out-of-phase radial velocities, e.g., v_p and $-v_p$ at the same time instant (say, t_{ei}). Note that such out-of-phase, radial velocities readily occur in flexural vibrational modes of thin shells — these flexural modes can have lower associated resonance frequencies than the totally symmetric breathing (fundamental) mode of vibration [19]. Consequently, photons emitted from these regions (at $t_{e,i}$) will arrive at the observer at different time instants (as in Eqs. 1.28, 1.29)

$$t_{o,i+} = t_{e,i} + \frac{d_{e,i} - r_p(0)}{c + c\beta_p(0)} \tag{1.36}$$

$$t_{o,i-} = t_{e,i} + \frac{d_{e,i} - r_p(0)}{c - c\beta_p(0)}. \tag{1.37}$$

This leads to a time shift $(t_{o,i-} - t_{o,i+})$ between the observed light from these two regions as illustrated in Fig. 1.6. The photon energy observed from each region can be different, and depends on the relative size (and energy-emission rate) of each region. Since light from both regions are observed simultaneously, the total light curve can show periodic changes that appear like binary systems. Moreover, two periodically-varying, apparent velocities (red shifts) will be observed as shown in Fig. 1.6 since the velocities (redshifts) of each region will be different. Such effects could account for large numbers of observed spectroscopic binaries with short time periods (associated with photosphere vibrations) even though visual binaries tend to have substantially-larger, time periods.

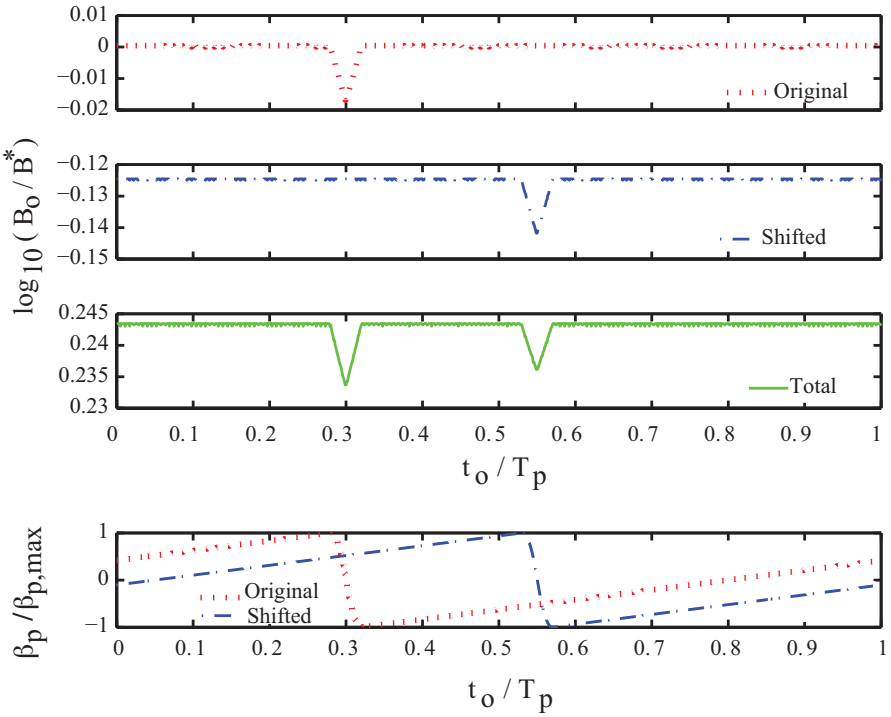

Figure 1.6: *Apparent binaries. (Top three plots) observed brightness B_o with bending modes of vibration in photosphere motion. The observed time shift (from the original brightness plot in Fig. 1.4) is a quarter of the time period ($T_p/4$) and the brightness of the shifted light curve is $3/4^{th}$ of the original brightness. (Bottom plot) observed photosphere speed ($\beta_p/\beta_{p,max}$), where at the same (shifted observer) time instant t_o, two values of photosphere speed can be observed, which could appear similar to observations from a spectroscopic binary.*

Remark 6 *Intermediate regions between the major vibrational regions will distort the simple addition of the two shifted light curves in Fig. 1.6; this distortion will depend on the relative size (and energy-emission rate) of the major and intermediate regions. Moreover, the spread of redshifts could lead a time-varying thickening of the spectrum bands rather than generating discrete values in the spectrum as in the above example. Such issues are not considered in this study, for simplicity.*

Remark 7 *Higher-order vibrational modes can lead to multiple regions with substantially different phase; this can lead to more than two, shifted, light curves being observed simultaneously — resulting in apparent multiple-star systems. These issues are not considered in this study, for simplicity. Nevertheless, the proposed Ritz-type model indicates that photosphere vibration can lead to observations that appear to be from binary or multi-star systems, that can explain current observations of large numbers of observed spectroscopic binaries with short time periods.*

1.5 Quasar Distance and Time Dilation

In this section, the cosmological expansion effect (that was neglected in the previous section, which studied nearby stars) is included when computing the time between emission and observation. The results are used to generate potential explanations for the apparent lack of time dilation in quasar light curves [6], as well as the observational links between quasars and nearby-galaxies [8, 9].

1.5.1 Time dilation expression

Consider the case when a photon is emitted by a moving photosphere, which is considered to be spherical about the emitter e as in Fig. 1.1. Let two photons be emitted at time instants $t_{e1} = t_{ei}$ and $t_{e2} = t_{ei} + t_e$, which reach the observer o at time instants t_{o1} and t_{o2} respectively. Since the center of the emitter is moving with speed $c - c_o$ away from the observer due to cosmological expansion in Eq. 1.6, during the emission time-interval $t_e = t_{e2} - t_{e1}$, the distance $d(e_1, o_1)$ (between the centers of the emitter and the observer) has increased by $V_{e,o}t_e = (c - c_o)\, t_e$ as illustrated in Fig. 1.7. Moreover, let the radius of the photosphere be $r_{p1} = r_p(t_{e1})$ and $r_{p2} = r_p(t_{e1})$ with expansion rates $c\beta_{p1} = c\beta_p(t_{e1})$ and $c\beta_{p2} = c\beta_p(t_{e2})$. Consequently, the photons emitted at time instants t_{e1} and t_{e2} move towards the observer at speeds $v_1 = c_o + c\beta_{p1}$ and $v_2 = c_o + c\beta_{p2}$.

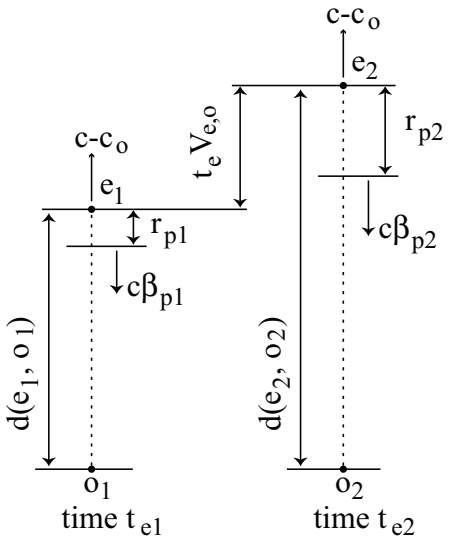

Figure 1.7: *Light emitted from point e_1 at time t_{e1} and from point e_2 at time $t_{e2} = t_{e1} + t_e$. The position of the photosphere is r_{p1} and r_{p2} away from the emitter (towards the observer) and the corresponding speeds of the photosphere are $c\beta_{p1}$ and $c\beta_{p2}$. The normalized speed $V_{e,o}$ of the emitter e with respect to the observer o is $c - c_o$. In the reference frame of the observer I_o, the location of the observer is fixed, i.e., $o_1 = o_2$.*

The arrival times for the photons at the observer are given by

$$t_{o1} = t_{e1} + \frac{d(e_e, o_e) - r_{p1}}{c_o + c\beta_{p1}} \tag{1.38}$$

$$t_{o2} = t_{e2} + \frac{d(e_e, o_e) + (c - c_o)t_e - r_{p2}}{c_o + c\beta_{p2}} \tag{1.39}$$

Therefore, the time interval t_o between observations is (provided $t_{o2} \geq t_{o1}$)

$$\begin{aligned} t_o(t_e) &= t_{o2} - t_{o1} \\ &= t_e + \frac{d(e_e, o_e) + (c - c_o)t_e - r_{p2}}{c_o + c\beta_{p2}} - \frac{d(e_e, o_e) - r_{p1}}{c_o + c\beta_{p1}} \\ &= t_e \left[1 + \frac{1 - c_o/c}{c_o/c + \beta_{p2}}\right] - \left[\frac{(\beta_{p2} - \beta_{p1})\,\frac{d(e_e,o_e)}{c}}{(c_o/c + \beta_{p2})(c_o/c + \beta_{p1})}\right] \\ &\quad - \left[\frac{\frac{r_{p2}}{c}}{c_o/c + \beta_{p2}} - \frac{\frac{r_{p1}}{c}}{c_o/c + \beta_{p1}}\right], \end{aligned} \tag{1.40}$$

which is similar to the expression (in Eq. 1.30) for the case without cosmological expansion in the previous section. The main difference between the two cases is in c_o/c term, e.g., in the first square bracket in Eq. (1.40) for the case with cosmological expansion — the differences vanish when the cosmological redshift is small, i.e., $c = c_o$ as in the derivation of Eq. (1.30). Moreover, the observation interval t_o becomes substantially large as the distance d_{e_1,o_1} increases and the second term in Eq. (1.40) dominates the expression — even for a small change in the photosphere speed over the emission interval t_e.

Remark 8 *Large changes in the observation time interval t_o can lead to redistributions of the light curve over the time period that can appear to be chaotic; similar advent of chaos has been studied in stellar dynamics, e.g., [20].*

The relation between emission and observation intervals in Eq. 1.40 can be rewritten in terms of the cosmological redshift z using Eqs. (1.4,1.11,1.12,1.21) as

$$\begin{aligned} t_o(t_e) &= t_e \left[1 + \frac{z}{1 + \beta_{p2}(1 + z)}\right] \\ &\quad - \left[\frac{H^{-1} z\,(\beta_{p2} - \beta_{p1})}{(1 + \beta_{p1}(1 + z))(1 + \beta_{p2}(1 + z))}\right] \\ &\quad - \left[\frac{(1 + z)\frac{r_{p2}}{c}}{1 + \beta_{p2}(1 + z)} - \frac{(1 + z)\frac{r_{p1}}{c}}{1 + \beta_{p1}(1 + z)}\right] \end{aligned} \tag{1.41}$$

Note that the second term in Eq. (1.41) relates to the speed variations in the photosphere and the third term includes radii variations of the photosphere.

Remark 9 *The time dilation in Eq. 1.41 collapses to the expression $t_o = (1 + z)t_e$ in Eq. (1.14) if the photosphere radius is not varying, i.e., ($r_{p1} = r_{p2}$) and speeds (β_{p1}, β_{p2}) are zero.*

1.5.2 Periodic pulse emissions

Consider the case, when emissions are periodic pulses occurring when the photosphere has a specific speed $c\beta_p$ and radius r_p — this could happen, for example, if the emission accompanies (periodic) collapses of the stellar system. Then the relation in Eq. (1.41) between the emission and observation time intervals (t_e, t_o) reduces to

$$t_o \;=\; t_e \left[1 + \frac{z}{1+\beta_p(1+z)}\right] \tag{1.42}$$

where z is the cosmological redshift. Note that this expression for time dilation (in Eq. 1.42) is similar to the standard time dilation expression (in Eq. 1.14) — the difference is the effect of the photosphere speed (i.e., β_p) at the instant the pulses are emitted.

1.5.3 Spectroscopic versus cosmological redshift

The time dilation can be expressed in terms of the measured redshift z_s (defined as the spectroscopic redshift) that includes the effect of photosphere motion, i.e., $\beta_p \neq 0$, rather than the redshift z (in Eq. 1.11) due to cosmological expansion alone without photosphere motion $\beta_p = 0$, where z is defined as the cosmological redshift. Towards this, the cosmological redshift z is compared with the spectroscopic redshift z_s that is given by (similar to Eq. 1.11)

$$1 + z_s \;=\; \frac{c}{c_o + c\beta_p} \tag{1.43}$$

provided

$$c_o + c\beta_p > 0, \tag{1.44}$$

which is important to ensure that emitted photons have a positive speed towards (and reach) the observer. The spectroscopic redshift z_s can be related to the cosmological redshift by using Eq. (1.11) as

$$1 + z_s \;=\; \frac{1}{\frac{1}{1+z} + \beta_p} \;=\; \frac{1+z}{1+\beta_p(1+z)}, \tag{1.45}$$

which can be rewritten as

$$(1+z) \;=\; \frac{(1+z_s)}{1-\beta_p(1+z_s)}. \tag{1.46}$$

The spectroscopic redshift z_s approaches infinity as the cosmological redshift z reaches a critical value z_c and the net speed of photons tends to zero. In particular, for photons to reach an observer, Eq. (1.44) should be satisfied, which also implies that the denominator of Eq. (1.46) should remain positive, i.e.,

$$(1+z)\beta_p > -1 \tag{1.47}$$

yielding an expression for the critical redshift z_c for a collapsing photosphere ($\beta_p < 0$) as

$$z < z_c = \frac{1}{|\beta_p|} - 1 \qquad \text{if } \beta_p < 0. \tag{1.48}$$

Remark 10 *Emitted photons would not be observed if the associated cosmological redshift z is greater than the critical redshift $z_c = \frac{-1}{\beta_p} - 1$ for a given collapsing photosphere speed $\beta_p < 0$.*

1.5.4 Distance to quasars

When the photosphere speed is small ($\beta_p \to 0$) the spectroscopic redshift z_s approaches the cosmological redshift z in Eq. (1.46). However, the spectroscopic redshift z_s can be large compared to the cosmological redshift z when $z \to z_c$ as seen in Fig. 1.8. Therefore, the Hubble law (Eq. 1.19) would indicate that an object is substantially further away if the spectroscopic redshift z_s is used instead of the cosmological redshift z. In other words, high spectroscopically-redshifted quasars might be nearer than previously thought, which could explain, e.g., the quasar redshift-distance anomalies such as potential links between high-(spectroscopic)-redshift quasars and lower-redshift galaxies [8, 9]. If the distance is not as large as thought, then it is possible that ejecta observations at superluminal speeds [12] might be traveling at much smaller speeds — although, the model presented here does not preclude superluminal speeds.

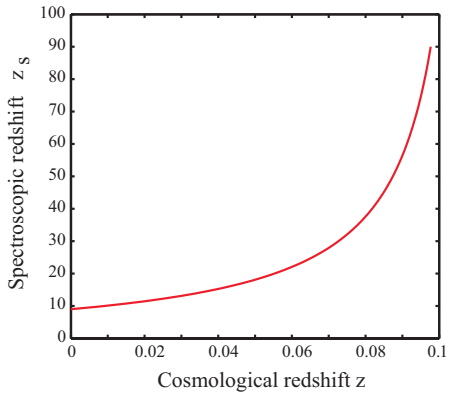

Figure 1.8: *Spectroscopic z_s versus cosmological z redshift with an example photosphere speed of $v_p = -0.9c$ ($\beta_p = -0.9$). This can lead to erroneous distance (and age) estimates from the Hubble law (Eq. 1.19) if the spectroscopic redshift z_s is used instead of the cosmological redshift z.*

1.5.5 Quasar time dilation

The time-dilation relation (in Eq. 1.42) between the emission and observation time intervals (t_e, t_o) can be expressed in terms of the spectroscopic redshift z_s as

$$\frac{t_o}{t_e} = \left[1 + \frac{\frac{z_s+\beta_p(1+z_s)}{1-\beta_p(1+z_s)}}{1+\beta_p\left(\frac{(1+z_s)}{1-\beta_p(1+z_s)}\right)}\right] = (1+z_s)\left[1+\beta_p\right]. \tag{1.49}$$

Therefore, the time dilation is smaller by $(1+\beta_p)$ when compared to the standard time-dilation expression obtained by replacing the cosmological redshift in Eq. (1.14) by the

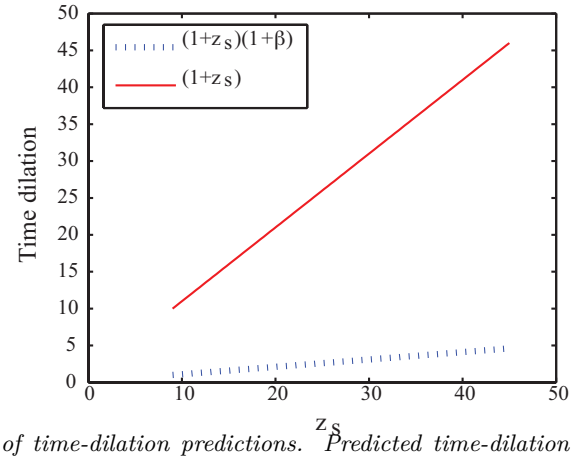

Figure 1.9: *Comparison of time-dilation predictions. Predicted time-dilation (solid line) based on the standard expression with spectroscopic redshift z_s as in Eq. (1.50) can be substantially higher than the predicted time-dilation (dotted line) based on the proposed model in Eq. (1.49). The difference depends on the photosphere speed, which is $v_p = -0.9c$ ($\beta_p = -0.9$) for this plot.*

spectroscopic redshift, i.e.,

$$\frac{t_o}{t_e} = (1 + z_s). \tag{1.50}$$

Thus, for a collapsing system, with large negative photosphere speeds, e.g., $\beta_p = -0.9$, the actual time dilation (from Eq. 1.49) can be substantially lower than the time dilation predicted by the standard expression (in Eq. 1.50) as seen in Fig. 1.9. This could explain analysis that appears to indicate that quasars do not show anticipated time dilation effects even with substantial spectroscopic redshifts [6].

Remark 11 *Emissions from quasar can have time dependency, which is different from the periodic pulses considered in the above analysis. Additionally, variations in the photosphere speeds can lead to more complex light curves (being observed) due to variations in the time dilation as predicted by Eq. (1.41) — these are not considered here for simplicity. Nevertheless, the above analysis shows the potential of the proposed model to account for the absence of time dilation in quasar light curves [6].*

Remark 12 *The difference between the spectroscopic redshift z_s and cosmological redshift z in the proposed model could explain the anomaly between smaller apparent distance (due to potential links to low redshift galaxies as well as the presence of superluminal ejecta) and large quasar (spectroscopic) redshifts [8, 9, 12].*

1.6 Consistency with Farther-Dimmer Effect

The effect of photosphere-speed variation is evaluated as a potential explanation of the farther-dimmer effect in supernovae observations [10].

1.6.1 Effect of speed variation on time dilation

Consider the case when the photosphere speed ($c\beta$) varies slightly over the time interval t_e. Then, the observed time dilation expression (Eq. 1.41) can be simplified, by setting $\beta_{p1} = \beta_p$, $\beta_{p2} = \beta_p + \alpha_p t_e$, and $\beta_{p2} - \beta_{p1} = \alpha_p t_e$, where α_p is the normalized photosphere acceleration. The overall photosphere changes are assumed to be small, i.e.,

$$1 + \beta_{p2}(1+z) \approx 1 + \beta_{p1}(1+z) \approx 1 + \beta_p(1+z) \tag{1.51}$$

and $r_{p2} \approx r_{p1} + c\beta_p t_e$ to obtain

$$\begin{aligned} t_o(t_e) &= t_e\left[1 + \frac{z}{1 + (\beta_p + \alpha_p t_e)(1+z)}\right] \\ &\quad - \left[\frac{H^{-1} z\,(\alpha_p t_e)}{(1+\beta_p(1+z))(1+(\beta_p + \alpha_p t_e)(1+z))}\right] \\ &\quad - \frac{(1+z)}{c}\left[\frac{r_{p1} + c\beta_p t_e}{1 + (\beta_p + \alpha_p t_e)(1+z)} - \frac{r_{p1}}{1+\beta_p(1+z)}\right] \\ &\approx t_e\left[1 + \frac{z}{1+\beta_p(1+z)}\right] \\ &\quad - \left[\frac{H^{-1} z\,(\alpha_p t_e)}{(1+\beta_p(1+z))(1+\beta_p(1+z))}\right] \\ &\quad - \frac{(1+z)}{c}\left[\frac{r_{p1} + c\beta_p t_e}{1+\beta_p(1+z)} - \frac{r_{p1}}{1+\beta_p(1+z)}\right] \end{aligned}$$

which can be simplified as

$$\begin{aligned} t_o(t_e) &= t_e\left[\frac{(1+\beta_p)(1+z)}{1+\beta_p(1+z)}\right] - \left[\frac{H^{-1} z \frac{(\alpha_p t_e)}{(1+\beta_p(1+z))}}{(1+\beta_p(1+z))}\right] - \left[\frac{(1+z)\beta_p t_e}{1+\beta_p(1+z)}\right] \\ &= t_e\left[\frac{(1+z)}{1+\beta_p(1+z)}\right] - \left[\frac{H^{-1} z \frac{(\alpha_p t_e)}{(1+\beta_p(1+z))}}{(1+\beta_p(1+z))}\right] \end{aligned} \tag{1.52}$$

i.e.,

$$t_o(t_e) = t_e(1+z)\left[\frac{1 - \frac{z}{1+z}\frac{\alpha_p H^{-1}}{(1+\beta_p(1+z))}}{1+\beta_p(1+z)}\right]. \tag{1.53}$$

1.6.2 Modified Hubble law

Substituting the modified time-dilation expression (Eq. 1.53) into the derivation of the observed brightness (i.e., in Eq. 1.17), the observed brightness of supernovae B_{SN} (B_o in Eq. 1.18) can be rewritten as

$$B_{SN} = \frac{L_e}{4\pi(\frac{Rc}{V})^2(\frac{z^2}{(1+z)})}\left(\frac{1+\beta_p(1+z)}{(1+z)\left[1-\frac{z}{1+z}\frac{\alpha_p H^{-1}}{(1+\beta_p(1+z))}\right]}\right) = \frac{L_e}{4\pi[d_{L,SN}]^2}, \quad (1.54)$$

with the following modified Hubble law (Eq. 1.19) for supernovae observations due to changes in the photosphere speed (represented by the term α_p)

$$d_{L,SN} = \frac{Rc}{V}z\sqrt{\left[\frac{1-\frac{z}{1+z}\frac{\alpha_p H^{-1}}{(1+\beta_p(1+z))}}{1+\beta_p(1+z)}\right]}, \quad (1.55)$$

where $d_{L,SN}$ is the luminosity distance for supernova observations. For small photosphere speeds (e.g., $\beta_p = 0.033$ [21]), the above expression can be simplified, further, to

$$d_{L,SN} \approx \frac{Rc}{V}z\sqrt{\left[1-\frac{z}{1+z}\alpha_p H^{-1}\right]}\ . \quad (1.56)$$

1.6.3 Farther dimmer with decelerating photosphere

If the photosphere acceleration is negative ($\alpha_p < 0$), then, the time dilation in Eq. (1.53) is increased — this results in an increase in the luminosity distance (e.g., in Eq. 1.56), and offers a potential explanation of the farther-dimmer effect [10], as discussed below.

Based on the Hubble law (Eq. 1.19), the variation of the observed (normalized) blue-band maximum μ_B from supernova (Type 1a) observations as a function of the host-galaxy redshift can be expressed in terms of the luminosity distance d_L (or, rather, the redshift z) as

$$\mu_B = K_B + 5\log_{10}\left[\frac{V}{Rc}d_L\right] = K_B + 5\log_{10}[z] \quad (1.57)$$

where K_B is a constant. This does not match the observed data from the Supernova Cosmology Project (SCP) [22] as shown in Fig. 1.10 — leading to the possibility of an accelerating universe.

With the proposed model, the variation of observed maximum light can be expressed in terms of the luminosity distance $d_{L,SN}$ as (from Eq. 1.55)

$$\begin{aligned}\mu_B &= K_B + 5\log_{10}\left[\frac{V}{Rc}d_L\right] \\ &= K_B + 5\log_{10}\left[z\left[\frac{1-\frac{z}{1+z}\frac{\alpha_p H^{-1}}{(1+\beta_p(1+z))}}{1+\beta_p(1+z)}\right]^{1/2}\right],\end{aligned} \quad (1.58)$$

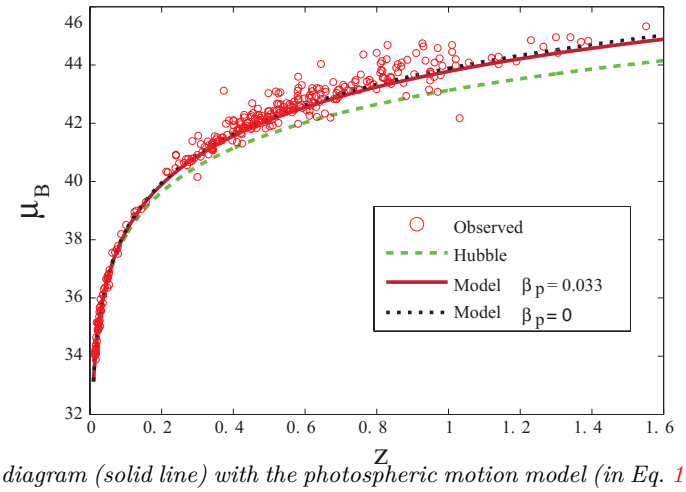

Figure 1.10: *Hubble diagram (solid line) with the photospheric motion model (in Eq. 1.55 with $\beta_p = 0.033$) captures the farther-dimmer relationship in supernova observations (circles) when compared to the predictions (dashed line) from the standard Hubble law (in Eq. 1.57). The prediction from the simplified model (in Eq. 1.59 with $\beta_p = 0$) is shown for comparison — the simplified prediction varies by less than 0.1 from the model with the nominal photospheric speed of $\beta_p = 0.033$. The circles represent 307 SNe data (that are not outliers) from the Supernova Cosmology Project (SCP) [22].*

which reduces to (at small photosphere speeds, $\beta_p \to 0$)

$$\mu_B(z) \quad = \quad K_B \; + 5\log_{10}\left[1 - \tfrac{z}{1+z}\alpha_p H^{-1}\right]. \tag{1.59}$$

The parameters $K_B = 43.13$ and $\alpha_p = -3.18H$ were estimated by minimizing the least square error between the model's prediction (from Eq. 1.58) and the observed data ($N_{SCP} = 307$ pairs of blue-band maximum and redshift $\mu_{B,i}, z_i$ with $i = 1$ to N_{SCP}) from the Supernova Cosmology Project (SCP) [22] at an example photosphere speed of $\beta_p = 0.033$ [21]. In particular, the residual error $E_{SCP,i}$ between the observed blue-band maximum $\mu_{B,i}$ and the predictions $\mu_B(z_i)$ (from Eq. 1.59) at the observed redshift z_i is defined as

$$E_{SCP,i} = \mu_{B,i} - \mu_B(z_i). \tag{1.60}$$

Moreover, the error norm E_{SCP} over all observations, given by

$$E_{SCP} = \sqrt{\sum_{i=1}^{N_{SCP}} \left[\mu_{B,i} - \mu_B(z_i)\right]^2}, \tag{1.61}$$

is plotted for different values of $K_B, \alpha_p H^{-1}$ in Fig. 1.11. The central ellipse in Fig. 1.11 represents the minimum of the error norm E_{SCP}, which led to parameter estimates of $K_B = 43.13$ and $\alpha_p = -3.18H$. The resulting residual error $E_{SCP,i}$ (Eq. 1.60) shown in Fig. 1.11 has low correlation with the redshift — the correlation $R_{residual}$ between the residual error $E_{SCP,i}$ and the redshift z_i is $R_{residual} = -0.0173$ with a 95% confidence interval $(-0.1290, 0.0948)$. Thus, the proposed model can account for the farther-dimmer relationship in supernova observations [10], without an accelerating universe.

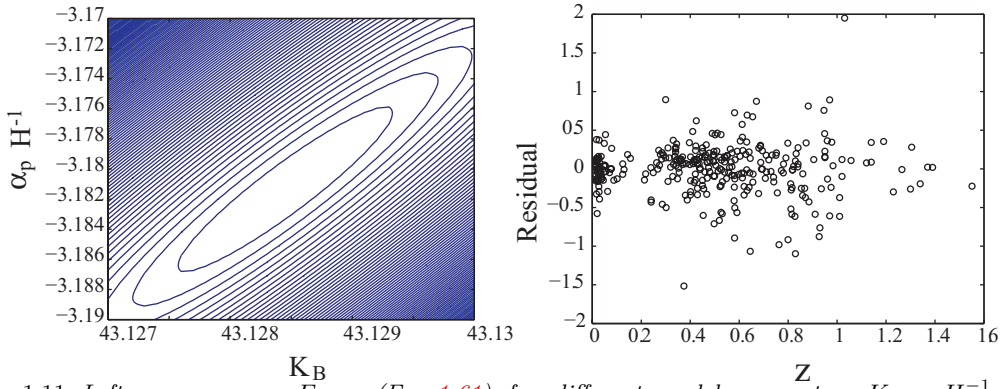

Figure 1.11: *Left: error norm E_{SCP} (Eq. 1.61) for different model parameters $K_B, \alpha_p H^{-1}$ from Eq. (1.59). The central ellipse in Fig. 1.11 represents the minimum of the error norm E_{SCP}, which led to parameter estimates of $K_B = 43.13$ and $\alpha_p = -3.18H$. Right: the resulting residual error $E_{SCP,i}$ (Eq. 1.60) has low correlation, $R_{residual} = -0.0173$, with redshift z_i.*

Remark 13 *Other, e.g., smaller, photosphere speeds are possible. The predicted Hubble diagram at small photosphere speeds (Eq. 1.59) is close to the prediction (Eq. 1.58) with the example photosphere speed of $\beta_p = 0.033$, as seen in Fig. 1.10.*

1.7 Temporal and Spatial Distortions

Variations in the speed of photons can cause temporal and spatial distortions in astronomical observations. Such distortions are discussed below for two cases: (i) temporal distortion in SNe light curves; and (ii) spatial distortion of mass distribution in galaxies.

1.7.1 Temporal distortion in SNe light curves

An aspect of the proposed model is the potential for apparent time reversal. In the previous Section 1.6.3, deceleration of the photosphere was shown to result in different photon speeds, which in turn, causes additional time dilation. A similar effect is possible, even with an accelerating photosphere due to apparent time reversal. In particular, a photon emitted at time t_{e2} could be observed earlier than a photon emitted earlier at time $t_{e1} < t_{e2}$ — let the corresponding observation times be t_{o1} (photon emitted earlier) and t_{o2} with $t_{o1} > t_{o2}$ as in Eq. (1.39). In this case, the time interval t_o between observations

is (reversing the observation time intervals t_{o1}, t_{o2}, in Eq. 1.40)

$$\begin{aligned} t_o(t_e) &= t_{o1} - t_{o2} \\ &= -t_e - \frac{d(e_e,o_e) + (c-c_o)t_e - r_{p2}}{c_o + c\beta_{p2}} + \frac{d(e_e,o_e) - r_{p1}}{c_o + c\beta_{p1}} \\ &= -t_e \left[1 + \frac{1 - c_o/c}{c_o/c + \beta_{p2}}\right] + \left[\frac{(\beta_{p2} - \beta_{p1})\,\frac{d(e_e,o_e)}{c}}{(c_o/c + \beta_{p2})(c_o/c + \beta_{p1})}\right] \\ &\quad + \left[\frac{\frac{r_{p2}}{c}}{c_o/c + \beta_{p2}} - \frac{\frac{r_{p1}}{c}}{c_o/c + \beta_{p1}}\right], \end{aligned} \tag{1.62}$$

which can be positive $t_o(t_e) > 0$ with an accelerating photosphere provided the second term in Eq. (1.62) is positive and dominates the other two terms in Eq. (1.62), i.e., the speed of the later photon β_{p2} is greater than the speed β_{p1} of earlier photon, there is sufficient travel distance $d(e_e, o_e)$ for the later photon to overtake the earlier photon, and there is no interference between the photons.

The apparent time reversal can lead to SNe light with the highest photosphere speeds to be observed first, with a continuous decrease in the observed photosphere speed over time — such a reduction in speed is present in SNe observations [21]. Moreover, if the photosphere was accelerating during the explosion, the apparent time reversal can lead to apparent reversal in the direction of the observed shock waves, i.e., they might appear to propagate backwards towards the supernova center. Further study is needed to evaluate if the reverse shock waves, seen in some of the SNe remnants [23], could be caused by such an effect. Finally, apparent time reversal also implies that light from the host galaxy (which might not have the large photosphere velocities as SNe) travel at a slower speed when compared to the associated SNe. Consequently, the light from the host galaxy (observed at the same time as the SNe) can be much older than the SNe. This difference in age (between SNe and their host galaxies) could account for the difficulty in identifying SNe progenitors [11].

1.7.2 Spatial distortion of astronomical structures

Variations in the arrival speed (of photons) can lead to distortions in the observed mass distribution of astronomical structures such as galaxies. If not accounted for, apparent spatial distortions can raise challenges in modeling the dynamics of observed physical phenomena such as the rotational dynamics of galaxies, which are dependent on the mass distribution. To illustrate, consider an astronomical structure, illustrated by the disc in Fig. 1.12 that is rotating about an axis EO that passes through the disc center E and is perpendicular to the disc. Consider light emitted from a point A on the disc, which is at a distance $r = d(E, A)$ from the disc center E with tangential speed $V_g(r) = c\beta_g(r)$. Let the observer be at location O, where the distance $d = d(E, O)$ is large compared to the radius r, which allows the approximation $d(A, O) \approx d$. Then, the time $t(r)$ for a

photon to travel to the observer at O is given by

$$t(r) = \frac{d(A,O)}{c_g} = \frac{d(A,O)}{c\sqrt{1-[\beta_g(r)]^2}} \approx \frac{d}{c\sqrt{1-[\beta_g(r)]^2}}, \tag{1.63}$$

where cosmological expansion effects are neglected in the relative speed of light c_g given by

$$c_g = c\sqrt{1-[\beta_g(r)]^2}. \tag{1.64}$$

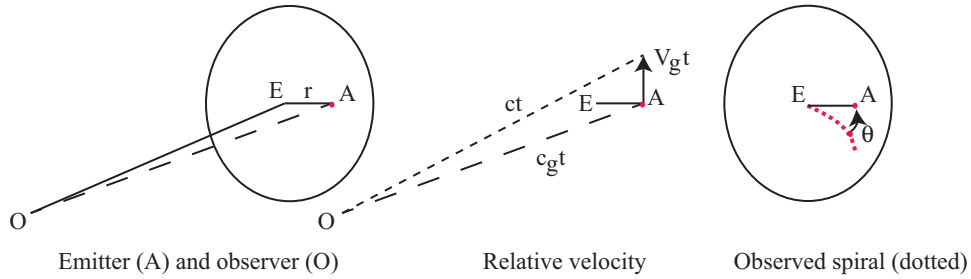

Figure 1.12: *Spiral spatial distortion. Travel times for emissions from A on a disc at radial distance r from the disc center E can vary with the radial distance d (as in Eq. 1.63) — this can lead to the straight segment EA appearing as a spiral when observed at O.*

The difference between the travel times for emission from the center E and the emission from the point A is given by

$$\Delta t(r) \;= t(r) - t(0) \;= \frac{d}{c\sqrt{1-[\beta_g(r)]^2}} - \frac{d}{c} \;= \frac{d}{c}\left[\frac{1-\sqrt{1-[\beta_g(r)]^2}}{\sqrt{1-[\beta_g(r)]^2}}\right]. \tag{1.65}$$

The above expression can be simplified, for small tangential speeds ($\beta_g(r) \to 0$), to

$$\Delta t(r) \;\approx \frac{d}{c}\left[\frac{[\beta_g(r)]^2}{2}\right]. \tag{1.66}$$

Note that the travel-time difference can be a function of the radial distance r from the center E, which can imply different angular rotations $\theta(r)$ before an emission reaches the observer. In particular, if the angular rotation rate $\omega(r)$ at each radius r is assumed to remain constant, then the time difference (in Eq. 1.66) corresponds to a rotation angle $\theta(r)$ given by

$$\theta(r) \;= \omega(r)\Delta t(r) \;= \frac{c\beta_g(r)}{r}\left[\frac{d}{c}\frac{[\beta_g(r)]^2}{2}\right] \;= \frac{d}{2r}[\beta_g(r)]^3. \tag{1.67}$$

If, for example, the disc rotates as a rigid body at a constant angular rate ω, then the tangential speed is given by

$$c\beta_g(r) \;= r\omega \tag{1.68}$$

and the corresponding angular rotation $\theta(r)$ during the travel time difference $\Delta t(r)$ is given by

$$\theta(r) \;=\; \frac{d}{2r}\left[\frac{r\omega}{c}\right]^3 \;\propto\; r^2. \tag{1.69}$$

Therefore, a straight line along the radius of the disc (e.g., EA) will appear to be a spiral due to increasing travel times for emissions along the length EA — as illustrated in Fig. 1.12. Such spatial distortion in observations needs to be corrected before studying the rotational dynamics since it can affect the mass distribution in the disc, and therefore, can affect the gravitational analysis.

Remark 14 *Similar spatial distortion can also occur along other directions such as the radial direction, e.g., in the presence of varying radial speeds if the disc collapses or expands, which will require further investigation.*

Remark 15 *The observed radial speeds would be influenced by the orientation of the galaxy with respect to the observer, which will further modify the observed shape.*

1.8 Geometry

The spherical-shell geometry allows for the total kinetic energy to be constant while satisfying momentum conservation. The implications and potential relaxation of this axiom are discussed below.

1.8.1 Peculiar velocities

The expansion rate is simplified to be a constant V (which maintains a constant kinetic energy) in the proposed cosmology model in contrast to a radial-distance-dependent speed variation as in Newtonian cosmology, e.g., [17]. Nevertheless, a small expansion-rate variation across the thickness of the shell could be included in the proposed cosmology model. For example, components on the outside of the shell will have a net gravitational force towards the center of the shell — in contrast, there would be no such force on components on the inside of the shell. Therefore, the speed V of the outer components in the shell (farther away from the center) is expected to reduce with respect to the inner components in the shell that are nearer to its center. Therefore, the inner components of the shell might appear to be attracted towards the outside components, which could explain observations such as peculiar velocities of galaxy clusters [24].

1.8.2 Anisotropy in cosmic microwave background radiation

The spherical shell geometry leads to variation between the radial and tangential directions. Moreover, even within the radial direction, there is anisotropy between the directions towards the center and away from the center. This should lead to anisotropy in observations such as the measured Hubble constant in different directions and in observations of the cosmic microwave background (CMB) radiation. Although, some

anisotropies have been reported in measurements of: (i) the Hubble constant, e.g., [25], and (ii) CMB radiation (e.g., quadrupole and octopole alignment [26,27]), further study is needed to check if such anisotropies are consistent with the proposed cosmology model.

1.8.3 Other geometries

If anisotropies in cosmological observations are not observed, then the proposed cosmology model can be considered without the spherical-shell geometry axiom. In this case, the Hubble law cannot be derived as in Section 1.3 under the proposed model. Therefore, the expansion of the cosmos should be considered as an axiom, as in current cosmology models. Nevertheless, the other results of the model, such as the explanation of apparent binaries in Section 1.4, the farther-dimmer effect in Section 1.6, and the temporal-and-spatial distortions in Section 1.7, would still be viable.

1.9 Chapter conclusions

This chapter developed a variable-speed-of-light (VSL) cosmology model and evaluated its potential to match current cosmological observations. It was shown that the proposed model can explain some of the anomalies in current cosmological observations. Additional work is needed to evaluate potential variations in the Hubble constant and anisotropies in the cosmic microwave background radiation due to differences between the radial and tangential directions in the spherical shell geometry to, both, test and potentially refine the model.

The source velocity augmentation axiom in the VSL model is controversial. A potential rationale for it is developed in the next chapter.

2 Relative-velocity-based electromagnetism

2.1 Overview

This chapter investigates if nonlinear relative-velocity-dependent (RV) models can be used to match standard relativity (SR) predictions, e.g., seen from cathode-ray-tube (CRT) experiments. The modeling approach is inspired by attempts at relative-velocity-dependent models in electromagnetism that were proposed by Weber [28,29] before data from CRT experiments were available. The model presented here also modifies prior work on relative-velocity dependent models in [16] to capture the relativistic speed-energy relationship observed in Van de Graaff electrostatic generators [30][1].

There are two major challenges in the development of relative-velocity-dependent models: (i) to capture standard relativisitic effects observed in, e.g., electromagnetism and optics; and (ii) to maintain model-invariance between inertial reference frames. The first challenge is addressed by modeling the nonlinearity of the proposed model to capture the mass increase seen in CRT experiments as well as the relativistic energy-speed relationship. The second challenge, to maintain model-invariance between different inertial frames, is addressed by developing relative-velocity dependent versions of Lorentz and Maxwell's equations, where spatial velocity distributions (V_E, V_B) are assigned to the electrical E and magnetic fields B. It is shown that Maxwell's equations, when adapted to include these relative-velocity distributions, are still co-ordinate invariant. What is noteworthy is that the relative-velocity approach models effects such as (i) the transverse Doppler effect and (ii) the convection of light by moving media (Fresnel drag) that typically required relativistic explanations.

2.2 Model

Consider a relative-velocity-based model of the Lorentz force F_E on a particle a with charge q and constant velocity V_a due to an electric field E (e.g., associated with a particle b) moving with constant velocity $V_E = V_b$ as in Fig. 2.1, with the following general form

$$F_E \;=\; [\mathcal{N}_\perp(V_{rel})]\, qE_\perp \;+ \left[\mathcal{N}_\parallel(V_{rel})\right] qE_\parallel, \tag{2.1}$$

where $E_\perp$ and $E_\parallel$ are the components of the field perpendicular and parallel to the relative velocity $V_{rel} = V_{a,E} = V_a - V_E$ between the field and the particle.

It is noted that ad-hoc choices of the nonlinearities ($\mathcal{N}_\perp, \mathcal{N}_\parallel$ in Eq. 2.1) are not acceptable. For example, instead of a relativistic, velocity-dependent increase in mass,

[1] Motivated by personal communication from Max Tran pointing out that the earlier model in [16] does not capture the results by Bertozzi in [30]

$m = m_0/\sqrt{1-\beta^2}$, seen in CRT experiments, a reduction of the perpendicular Lorentz force, such as $\mathcal{N}_\perp = \sqrt{1-\beta^2}$, might be considered, where c is the speed of light, m_0 is the rest mass and $\beta = |V_{rel}|/c$ is the normalized speed. However, it is shown that such a nonlinearity is not consistent with Ampere's law for the force between two current-carrying wires. In contrast, the proposed relative-velocity-based models capture low-velocity effects such as the force between two current carrying wires.

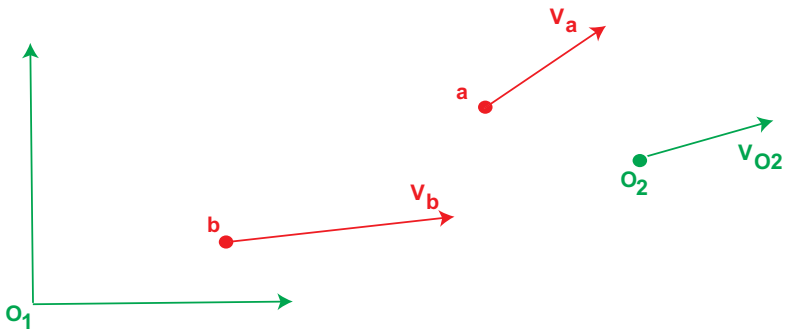

Figure 2.1: Force on a particle a with velocity V_a with respect to (wrt) observer O_1 due to fields generated by particle b with velocity V_b wrt observer O_1. Another potential observer is O_2 moving with constant velocity V_{O2} wrt to observer O_1.

2.2.1 Perpendicular nonlinearity $\mathcal{N}_\perp$

The perpendicualr nonlinearity $\mathcal{N}_\perp$ (in Eq. 2.1) is identified using (i) low speed effects (energy density invariance) and (ii) high speed (CRT) effects as in [16].

Low-speed, relative-velocity (RV) modeling of magnetic field

The Lorentz force F_B on a particle a with charge q and constant velocity V_a due to a magnetic field (e.g., associated with a particle b) moving with constant velocity $V_B = V_b$ as in Fig. 2.1, is modeled as

$$F_B \;=\; q\,(V - V_B) \times B. \tag{2.2}$$

This is effectively an electric field E_B, perpendicular to the relative velocity $V - V_B$

$$E_B \;=\; (V - V_B) \times B, \tag{2.3}$$

which results in a field energy that varies with the relative velocity of the charged particle $V_{rel} = V_a - V_B$. The net energy can be made independent of the relative velocity V_{rel}, if the apparent magnetic field B_B is reduced in the perpendicular direction, as

$$B_B \;=\; B_{\|} \;+ \gamma_B B_\perp \tag{2.4}$$

where $\gamma_B B_\perp$ is the vector component of magnetic field perpendicular to the relative velocity $(V - V_B)$, and $B_{\|}$ is the vector component of the magnetic field parallel to relative velocity $(V - V_B)$.

Remark 16 (Energy balance) *In the nominal case, when the relative velocity is zero, i.e., $V = V_B$, with no change in the perpendicular component, the factor $\gamma_B = 1$. When the relative velocity is nonzero, the factor γ_B is chosen such that the net energy density of B_B and E_B (due to the magnetic field B) is independent of the relative velocity $(V - V_B)$.*

Matching the energy density in the field's perpendicular component to the case when the relative velocity is zero, results in

$$\frac{\gamma_B^2}{2\mu}|B_\perp|^2 + \frac{\epsilon}{2}|E_B|^2 = \frac{1}{2\mu}|B_\perp|^2, \tag{2.5}$$

where $|\cdot|$ represents the magnitude of a vector, ϵ is the permittivity, and μ is the permeability. Substituting for the apparent electric field E_B from Eq. (2.3), i.e.,

$$E_B = (V - V_B) \times B = (V - V_B) \times B_\perp, \tag{2.6}$$

into Eq. (2.5), yields

$$\frac{\gamma_B^2}{2\mu}|B_\perp|^2 + \frac{\epsilon\,|V - V_B|^2}{2}|B_\perp|^2 = \frac{1}{2\mu}|B_\perp|^2 \tag{2.7}$$

and

$$\gamma_B = \sqrt{1 - \frac{|V - V_B|^2}{c^2}} = \sqrt{1 - \beta_B^2}\ , \tag{2.8}$$

where $c = \sqrt{1/\epsilon\mu}$ is the speed of light and β_B is the normalized normalized speed

$$\beta_B = |V - V_B|/c. \tag{2.9}$$

Low-speed, relative-velocity modeling of electric field

Similarly, an electric field E appears to have an effective magnetic field B_E, perpendicular to the relative velocity $V - V_E$, where

$$B_E = -\epsilon\mu(V - V_E) \times E \tag{2.10}$$

where the term $-\epsilon\mu$ is used in Eq. (2.10) to match the magnetic field produced by a current-carrying wire (Ampere's law). In particular, if ρ (charge per unit length) is flowing with velocity v through a wire (which is stationary in the reference frame O) then the electric field E_ρ associated with this charge, at a distance $r\hat{r}$ from the wire, is given by $E_\rho = [\rho/(2\pi\epsilon r)]\hat{r}$, where $\hat{r}$ represents a unit direction vector. Note that the velocity associated with this electric field is the velocity v of the charge flowing through the wire. Therefore, from Eq. (2.10), the magnetic field B_ρ at a distance $r\hat{r}$ from the wire is

$$\begin{aligned} B_\rho &= -(\epsilon\mu)\ (0 - v) \times E_\rho = (\epsilon\mu)\ v \times E_\rho \\ &= \epsilon\mu[\rho/(2\pi\epsilon r)]|v| \quad \hat{v} \times \hat{r} \\ &= [\mu I/(2\pi r)] \quad \hat{v} \times \hat{r} \end{aligned} \tag{2.11}$$

where I is the current in the wire; this is the expression for magnetic field produced by a current-carrying wire. Again, to keep the net energy independent of the relative velocity $V - V_E$, the following reduction γ_E in the perpendicular direction of the apparent electric field E_E is considered

$$E_E \;=\; E_{\parallel} \;+ \gamma_E E_{\perp} \tag{2.12}$$

where $\gamma_E E_{\perp}$ is the vector component of electric field perpendicular to the relative velocity $(V - V_E)$, and $E_{\parallel}$ is the vector component of the electric field parallel to relative velocity $(V - V_E)$.

Remark 17 (Energy balance) *Similar to the previous case for magnetic fields, when the relative velocity is nonzero, the scaling factor γ_E is chosen such that the net energy density of the fields E_E and B_E (due to the moving electric field E) is independent of the relative velocity $(V - V_E)$.*

The factor γ_E is obtained by equating the total energy density to the energy density when the relative velocity is zero as

$$\frac{\epsilon \gamma_E^2}{2}|E_{\perp}|^2 \;+ \frac{1}{2\mu}|B_E|^2 \;=\; \frac{\epsilon}{2}|E_{\perp}|^2. \tag{2.13}$$

Substituting for the apparent magnetic field B_E from Eq. (2.10), i.e.,

$$B_E \;=\; -\epsilon\mu(V - V_E) \times E \;=\; -\epsilon\mu(V - V_E) \times E_{\perp}, \tag{2.14}$$

into Eq. (2.13), yields

$$\frac{\epsilon \gamma_E^2}{2}|E_{\perp}|^2 \;+ \frac{\epsilon^2\mu^2\,|V - V_E|^2}{2\mu}|E_{\perp}|^2 \;=\; \frac{\epsilon}{2}|E_{\perp}|^2 \tag{2.15}$$

and a scaling factor

$$\gamma_E \;=\; \sqrt{1 - \frac{|V - V_E|^2}{c^2}}\;. \tag{2.16}$$

In summary, the net force on an electric particle (of charge q) is given by [from equations (2.2, 2.10) and (2.12)]

$$\begin{aligned} F_E \;&=\; q\,(V - V_E) \times B_E \;+ qE_{\parallel} \;+ q\gamma_E E_{\perp} \\ &=\; q\,(V - V_E) \times \{-\epsilon\mu(V - V_E) \times E\} \;+ qE_{\parallel} \;+ q\gamma_E E_{\perp} \\ &=\; q\tfrac{|V - V_E|^2}{c^2}E_{\perp} \;+ qE_{\parallel} \;+ qE_{\perp}\sqrt{1 - \tfrac{|V - V_E|^2}{c^2}} \\ &=\; q\left[\beta_E^2 \;+ \sqrt{1 - \beta_E^2}\right]E_{\perp} \;+ qE_{\parallel} \\ &=\; q\alpha E_{\perp} \;+ qE_{\parallel} \end{aligned} \tag{2.17}$$

where the normalized normalized speed β_E and the scaling factor α are given by

$$\beta_E = |V - V_E|/c \;\text{ and }\; \alpha = \beta_E^2 \;+ \sqrt{1 - \beta_E^2}\;. \tag{2.18}$$

Remark 18 (Similarity of scaling factor) *The expression for the scaling factor γ_E for the moving electric field E in Eq. (2.16) is similar to the one for the scaling factor γ_B for a moving magnetic field B in Eq. (2.8).*

Capturing high-speed effects with the relative-velocity model

The relativistic mass dependence with speed is modeled as a slip effect, where the force on the particle reduces as the relative-velocity increases. In particular, consider the augmentation of the Lorentz force on an electric particle, in Eq. (2.17), with relative-velocity terms $s_\perp$ and $s_\parallel$ to obtain the general nonlinear Eq. (2.1) as

$$\begin{aligned} F_E &= [\mathcal{N}_\perp(V_{rel})]\, qE_\perp + \left[\mathcal{N}_\parallel(V_{rel})\right] qE_\parallel \\ &= [s_\perp(\beta_E)]\, q\alpha E_\perp + \left[s_\parallel(\beta_E)\right] qE_\parallel = F_{E,\perp} + F_{E,\parallel}. \end{aligned} \tag{2.19}$$

Remark 19 (Slip terms for magnetic fields) *Similar to the electric field case in Eq. consider the augmentation of The Lorentz force on an electric particle, due to a magnetic field in Eq. (2.2) can be modelled in a similar manner with relative-velocity term $s_\perp$ as the electric field in Eq. (2.19), i.e.,*

$$F_B = [s_\perp(\beta_B)]\, q(V - V_B) \times B_\perp \tag{2.20}$$

Remark 20 (Matching relativistic mass gain) *The perpendicular slip term $s_\perp$ is identified by matching results from cathode-ray-tube (CRT) observations.*

Consider the forces on a charge q moving with velocity V perpendicular to stationary magnetic B and electric E fields, as in cathode-ray-tube (CRT) experiments (Thomson 1897), found from Eqs. (2.19, 2.20), as

$$F_B = s_\perp(\beta)\; q\; V \times B \tag{2.21}$$

$$F_E = s_\perp(\beta)\; \alpha(\beta)\; q\; E \tag{2.22}$$

where $\beta = \frac{|V|}{c}$. If the fields act on the charged CRT particle over some length L, then the change in velocity of the CRT particle along the application of the force during the time interval $\Delta t = L/|V|$ is given by

$$\frac{F_B L}{m|V|} \quad \text{and} \quad \frac{F_E L}{m|V|}$$

where m is the mass of the particle (electron). Therefore, the change in angles (θ_B and θ_E) of the CRT particle's path along the action of the fields B and E, respectively, can be approximated by using equations (2.21, 2.22) as [31]

$$\theta_B = |\frac{F_B L}{m|V|^2}| = \frac{s_\perp(\beta)\; q\; |V|\; |B|\; L}{m|V|^2} = \frac{s_\perp(\beta)\; |B|\; L}{\frac{m}{q}|V|} \tag{2.23}$$

$$\theta_E = |\frac{F_E L}{m|V|^2}| = \frac{s_\perp(\beta)\; \alpha(\beta)\; |E|\; L}{\frac{m}{q}|V|^2}. \tag{2.24}$$

In the absence of the relative-velocity terms (i.e., $s_\perp(\beta) = 1$ and $\alpha(\beta) = 1$), a velocity-dependent mass variation can be used to explain the CRT data. In particular, the estimated velocity V_{CRT} and the estimated mass-to-charge ratio

$$\frac{m(\beta_{CRT})}{q} = \frac{m}{q}\ \Psi(\beta_{CRT}),$$

with

$$\beta_{CRT} = \frac{|V_{CRT}|}{c}, \tag{2.25}$$

from the CRT experiments would be related by

$$\theta_B \ = \ \frac{|B|\ L}{\frac{m}{q}\Psi(\beta_{CRT})|V_{CRT}|} \tag{2.26}$$

$$\theta_E \ = \ \frac{|E|\ L}{\frac{m}{q}\Psi(\beta_{CRT})|V_{CRT}|^2} \tag{2.27}$$

where $\Psi(\beta_{CRT})$ represents the CRT-predicted variation of mass with velocity. Dividing equations (2.23) and (2.24) by equations (2.26) and (2.27), respectively, yields

$$s_\perp(\beta) \ = \ \frac{|V|}{|V_{CRT}|}\ \frac{1}{\Psi(\beta_{CRT})} \tag{2.28}$$

$$s_\perp(\beta)\ \alpha(\beta) \ = \ \frac{|V|^2}{|V_{CRT}|^2}\ \frac{1}{\Psi(\beta_{CRT})}. \tag{2.29}$$

The velocity V_{CRT} predicted by the CRT-experiments can be obtained by dividing Eq. (2.28) by Eq. (2.29) to obtain

$$|V_{CRT}| = \frac{|V|}{\alpha(\beta)} \quad \text{or} \quad \beta_{CRT} = \frac{\beta}{\alpha(\beta)}. \tag{2.30}$$

Furthermore, the perpendicular-slip term $s_\perp(\beta)$ can be found by dividing the square of Eq. (2.28) by Eq. (2.29) and then substituting for β_{CRT} from Eq. (2.30) to obtain

$$s_\perp(\beta) = \frac{\alpha(\beta)}{\Psi(\beta_{CRT})} \ = \frac{\alpha(\beta)}{\Psi(\frac{\beta}{\alpha(\beta)})}. \tag{2.31}$$

Case 1: matching the relativistic mass-velocity relation: The perpendicular term $s_\perp(\beta)$ can be chosen, as in Eq. (2.31), to exactly match the observed velocity-dependent variation Ψ in mass. In particular, if the CRT-predicted mass increase is given by the relativistic expression

$$\Psi(\beta_{CRT}) = \frac{1}{\sqrt{1-\beta_{CRT}^2}}, \tag{2.32}$$

then the expression for the slip term $s_\perp$ is obtained, from Eq. (2.30) and Eq. (2.31), as

$$\begin{aligned} s_\perp(\beta) &= \alpha(\beta) \left\{ \sqrt{1 - \left[\frac{\beta}{\alpha(\beta)}\right]^2} \right\} \\ &= \sqrt{[\alpha(\beta)]^2 - \beta^2}. \end{aligned} \tag{2.33}$$

Case 2: simplified perpendicular slip term: Consider the following, simplified expression $\bar{s}_\perp$ for the slip term $s_\perp(\beta)$

$$\bar{s}_\perp(\beta) = \left[1 - \beta^8\right]^{1/4}, \tag{2.34}$$

which closely approximates the perpendicular slip term $s_\perp$ in Eq. (2.33) needed to match the relativistic mass increase, as shown in Fig. 2.2.

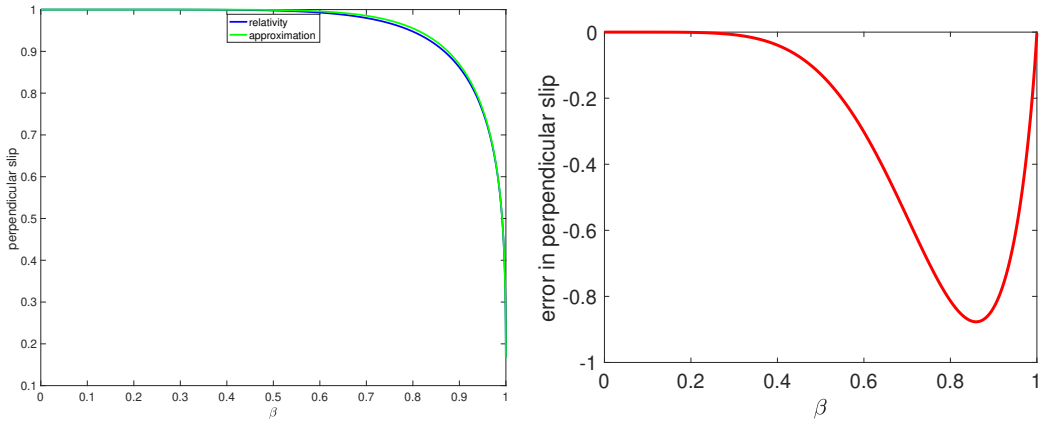

(a) (b)

Figure 2.2: (a) The approximate perpendicular slip term $\bar{s}_\perp$ in Eq. (2.34), shown in green, closely matches the perpendicular slip term $s_\perp$ in Eq. (2.33), shown in blue, needed to match the relativistic mass increase. (b) The magnitude of the percent difference $100 \times (s_\perp - \bar{s}_\perp)/s_\perp$ in the approximation is less than 1%.

The approximate slip term does not lead to an exact match of the relativistic mass increase; however, it closely approximates the expression for the relativistic mass increase. In particular, assuming this form $\bar{s}_\perp(\beta)$ for the slip term, the velocity $\bar{\beta}_{CRT}$ estimated in the CRT experiment, as in Eq. (2.30), is given by

$$\bar{\beta}_{CRT} = \frac{\beta}{\alpha(\beta)} = \frac{\beta}{\beta^2 + \sqrt{1 - \beta^2}}. \tag{2.35}$$

Moreover, the apparent mass variation $\bar{\Psi}$ in the CRT experiment, as in Eq. (2.31), is given by

$$\bar{\Psi}(\bar{\beta}_{CRT}) = \frac{\alpha(\beta)}{s(\beta)} = \frac{\beta^2 + \sqrt{1 - \beta^2}}{[1 - \beta^8]^{1/4}}. \tag{2.36}$$

It is noted that the variation of $\bar{\Psi}(\bar{\beta}_{CRT})$ with velocity $\bar{\beta}_{CRT}$ in equations (2.35, 2.36), which would be obtained from a CRT experiment, is similar to the relativistic variation

$$\Psi(\bar{\beta}_{CRT}) = \frac{1}{\sqrt{1-\bar{\beta}_{CRT}^2}}, \tag{2.37}$$

as shown in Fig. 2.3. Moreover, the percentage difference Ψ_{error} between the two expressions (equations 2.36 and 2.37) given by

$$\Psi_{error} = \frac{\Psi(\bar{\beta}_{CRT}) - \bar{\Psi}(\bar{\beta}_{CRT})}{\Psi(\bar{\beta}_{CRT})} \times 100 \tag{2.38}$$

is less than 1% as shown in Fig. 2.3. Thus, the relativistic velocity dependency of mass in CRT experiments can be modeled using the relative-velocity approach with the perpendicular nonlinearity ($\mathcal{N}_\perp = s_\perp \alpha$) in the Lorentz force expression and a constant mass as in Eq. (2.19).

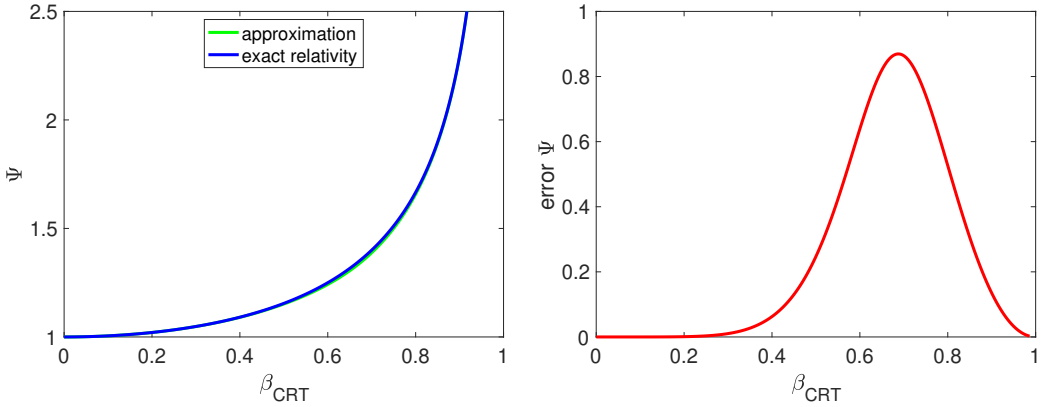

(a) (b)

Figure 2.3: Proposed model matches the apparent velocity dependence of mass in CRT experiments. Left plot: comparison of apparent mass variations $\Psi(\bar{\beta}_{CRT})$ (relativistic mass model) and $\bar{\Psi}(\bar{\beta}_{CRT})$ (simplified model) as in Eqs. (2.36, 2.37) with normalized normalized speed $\bar{\beta}_{CRT}$ in Eq. (2.35). Right plot: the difference Ψ_{error} in predicted mass variation is less than 1% with the simplified model in Eq. (2.38). There would be no error with the exact relative-velocity model in Eq. (2.33).

2.2.2 Parallel nonlinearity $\mathcal{N}_\parallel$

The parallel nonlinearity $\mathcal{N}_\parallel$ (in Eq. 2.1) is identified using relativistic energy and velocity relationship, e.g., observed in [30] and keeping the potential energy independent of speed.

Relationship between parallel slip and kinetic energy

Consider a charged particle q moving along a straight line away from a stationary charged particle Q at a distance $r\hat{r}$ as shown in Fig. 2.4 (case 1).

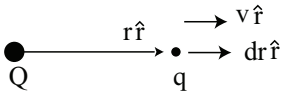

Figure 2.4: Example with force parallel direction $\hat{r}$ to the relative velocity.

Taking the dot product with a small displacement $dr\hat{r}$ with Newton's law on the charge q yields

$$s_{\parallel}(\beta)\frac{Qq}{4\pi\epsilon r^2}dr \;=\; m\frac{dv}{dt}dr \;=\; \frac{m}{2}dv^2 \;=\; \frac{mc^2}{2}d\beta^2. \tag{2.39}$$

Dividing both sides by the parallel slip term $s_{\parallel}(\beta)$ and integrating results in

$$\int_{r_1}^{r_2}\frac{Qq}{4\pi\epsilon r^2}dr \;=\; \int_{\beta_1^2}^{\beta_2^2}\frac{mc^2}{2s_{\parallel}(\beta)}d\beta^2 \;=\; \int_{\mathcal{E}_{KE,1}}^{\mathcal{E}_{KE,2}}\frac{d\mathcal{E}_{KE}}{d\beta^2}d\beta^2 \tag{2.40}$$

where $\mathcal{E}_{KE}$ is considered as the relative-velocity dependent kinetic energy of the system since the above expression leads to the conservation law

$$\frac{Qq}{4\pi\epsilon r_2}+\mathcal{E}_{KE,2} \;=\; \frac{Qq}{4\pi\epsilon r_1}+\mathcal{E}_{KE,1}, \tag{2.41}$$

in which the potential energy expression $Qq/(4\pi\epsilon r)$ is independent of the relative velocity and the parallel slip term $s_{\parallel}(\beta)$. Then, the relationship between the parallel slip term and the kinetic energy becomes (from Eq. 2.40)

$$\frac{d\mathcal{E}_{KE}}{d\beta^2} \;=\; \frac{mc^2}{2s_{\parallel}(\beta)}, \tag{2.42}$$

resulting in the parallel slip expression,

$$s_{\parallel}(\beta) \;=\; \frac{mc^2}{2}\frac{1}{\frac{d\mathcal{E}_{KE}}{d\beta^2}}. \tag{2.43}$$

Remark 21 (Potential energy independence) *The parallel slip term $s_{\parallel}$ in Eq. (2.43) was developed assuming that the potential energy (PE) is independent of speed β. Other forms could be generated if PE is assumed to depend on the speed.*

2.2.3 Matching relativistic energy

If the kinetic energy ($\mathcal{E}_{KE}$) depends on the normalized speed β according to the relativistic expression

$$\mathcal{E}_{KE}=\frac{mc^2}{\sqrt{1-\beta^2}}-mc^2, \tag{2.44}$$

with

$$\frac{d\mathcal{E}_{KE}}{d\beta^2} \;=\; \frac{mc^2}{2}\frac{1}{\sqrt{(1-\beta^2)^3}}. \tag{2.45}$$

Then, the parallel slip term to match the relativistic KE in Eq. (2.44) can be found from Eq. (2.43) and Eq. (2.45) as

$$s_{\parallel}(\beta) = \sqrt{(1-\beta^2)^3}. \tag{2.46}$$

Remark 22 (Matching relativistic energy expression) *The parallel slip term $s_{\parallel}$ matches the relativistic energy and velocity relationship in Eq. (2.44) and observed by Bertozzi in [30].*

2.3 Relative-velocity-dependent Lorentz force

The relative-velocity-dependent Lorentz force in Eq. (2.19), with $\beta_E = \beta$, becomes from Eqs. (2.18, 2.33, 2.46),

$$\begin{aligned} F_E &= [\mathcal{N}_{\perp}(V_{rel})]\, qE_{\perp} + [\mathcal{N}_{\parallel}(V_{rel})]\, qE_{\parallel} \\ &= [s_{\perp}(\beta)]\, \alpha(\beta) qE_{\perp} \\ &= \left(\sqrt{\left[\beta^2 + \sqrt{1-\beta^2}\right]^2 - \beta^2}\right)\left(\beta^2 + \sqrt{1-\beta^2}\right) qE_{\perp} + \left[\sqrt{(1-\beta^2)^3}\right] qE_{\parallel}. \end{aligned} \tag{2.47}$$

When the relative velocity β is small, the above Lorentz-force expression in Eq. (2.47) can be approximated by (using Taylor series expansion)

$$F_E \approx \left(1 + \frac{1}{2}\beta_E^2\right) qE_{\perp} + \left(1 - \frac{3}{2}\beta_E^2\right) qE_{\parallel}. \tag{2.48}$$

Remark 23 (Saturation effect) *The above analysis is limited to the case when the magnitude of the relative velocity is less than the speed of light c, i.e., $\beta_E \leq 1$ and $\beta_B \leq 1$. The approach could be extended to higher-normalized speeds by saturating the scaling factors, e.g.,*

$$\gamma_E = 1 \;\; \forall\; \beta_E > 1, \qquad \gamma_B = 1 \;\; \forall\; \beta_B > 1. \tag{2.49}$$

In the following, it is assumed that $\beta_E \leq 1$ and $\beta_B \leq 1$.

Remark 24 (Coordinate independence) *The normalized speed of particle a with respect to particle b does not change for observers O_1 and O_2 in Fig. 2.1. Therefore, the relative-velocity-dependent Lorentz force expression in Eq. (2.47) is coordinate independent.*

2.4 Force between two wires

The relative-velocity-dependent Lorentz force expression predicts the observed force between two current carrying wires. In particular, the increase in the electrical force

component perpendicular to the relative velocity in Eq. (2.48) can be used to explain the force between two current carrying wires, which are both stationary in a reference frame O. As shown in Fig. 2.5, let the second wire (denoted by the subscript 2) be positioned at $r\hat{r}$ from the first wire (denoted by the subscript 1). Moreover, let the currents in the two parallel wires be I_1 and I_2, and let the corresponding moving charges (per unit length) be $-\rho_1$ and $-\rho_2$ with velocities $-v_1\hat{V}$ and $-v_2\hat{V}$, respectively, i.e.,

$$I_1 = \rho_1 v_1, \text{ and } I_2 = \rho_2 v_2 \tag{2.50}$$

where the speeds $v_1 \geq 0$ and $v_2 \geq 0$ of the charges are small, and $\hat{V}$ is a unit vector along the direction of the wire (in which current is flowing).

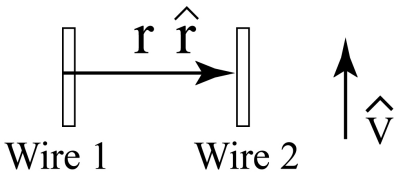

Figure 2.5: Force between two current carrying parallel wires separated by distance r.

Force expression

Consider the two (non-canceling) fields in the first wire: (a) $E_{-\rho_1}$ associated with the moving charges ($-\rho_1$ per unit length) with field velocity $-v_1\hat{V}$ given by (using Gauss's law, $E_{-\rho_1}(2\pi rL) = (-\rho)L/\epsilon$ for length L of the charged wire)

$$E_{-\rho_1} = [-\rho_1/(2\pi\epsilon r)]\hat{r}; \tag{2.51}$$

and (b) E_{ρ_1} associated with the corresponding stationary charges (ρ_1 per unit length) in the wire, i.e., the stationary field given by

$$E_{\rho_1} = [\rho_1/(2\pi\epsilon r)]\hat{r}. \tag{2.52}$$

These two fields act on the moving charges ($-\rho_2$ per unit length) and the corresponding stationary charges (ρ_2 per unit length) on the second wire. For example, the force per unit length $F_{-\rho_1,-\rho_2}$ on the moving charges $-\rho_2$ due to the moving charges $-\rho_1$ can be obtained from equations (2.48, 2.51) as

$$\begin{aligned} F_{-\rho_1,-\rho_2} &= -\rho_2 \left(1 + \tfrac{|(-v_2)-(-v_1)|^2}{2c^2}\right) E_{-\rho_1} \\ &= -\rho_2 \left(1 + \tfrac{|(-v_2)-(-v_1)|^2}{2c^2}\right) [-\rho_1/(2\pi\epsilon r)]\hat{r} \\ &= \tfrac{\rho_1\rho_2\hat{r}}{2\pi\epsilon r}\left(1 + \tfrac{|v_1-v_2|^2}{2c^2}\right). \end{aligned} \tag{2.53}$$

Similarly, (i) the force per unit length $F_{\rho_1,-\rho_2}$ on the moving charges $-\rho_2$ due to the stationary charge ρ_1, as well as (ii) the the forces $F_{-\rho_1,\rho_2}, F_{\rho_1,\rho_2}$ on the stationary charges

ρ_2 on the second wire due to the charges (on the first wire) $-\rho_1$ and ρ_1, respectively, are given by

$$\begin{aligned} F_{\rho_1,-\rho_2} &= -\frac{\rho_1\rho_2\hat{r}}{2\pi\epsilon r}\left(1+\frac{|-v_2|^2}{2c^2}\right) \\ F_{-\rho_1,\rho_2} &= -\frac{\rho_1\rho_2\hat{r}}{2\pi\epsilon r}\left(1+\frac{|v_1|^2}{2c^2}\right) \\ F_{\rho_1,\rho_2} &= \frac{\rho_1\rho_2\hat{r}}{2\pi\epsilon r}\,. \end{aligned} \tag{2.54}$$

Thus, the total force per unit length $F_{1,2}$ on the second wire can be found using equations (2.53, 2.54) as

$$\begin{aligned} F_{1,2} &= F_{\rho_1,\rho_2}+F_{\rho_1,-\rho_2}+F_{-\rho_1,\rho_2}+F_{-\rho_1,-\rho_2} \\ &= \frac{\rho_1\rho_2\hat{r}}{2\pi\epsilon r}\left[1-\left(1+\frac{|v_2|^2}{2c^2}\right)-\left(1+\frac{|v_1|^2}{2c^2}\right)+\left(1+\frac{|v_1-v_2|^2}{2c^2}\right)\right] \\ &= \frac{\rho_1\rho_2\hat{r}}{2\pi\epsilon r}\left(\frac{-2v_1v_2}{2c^2}\right) \quad = \quad -\frac{\mu I_1 I_2}{2\pi r}\hat{r}. \end{aligned} \tag{2.55}$$

This force on the second wire is attractive (i.e., towards the first wire) when the two wires carry current in the same direction.

Force between wires is incorrect with ad-hoc perpendicular slip term

Another choice of the perpendicular slip term can be found by matching the acceleration resulting from the relativistic increase in mass with speed. For example, the slip term $s_\perp(\beta_E)$ in Eq. (2.19) can be chosen such that the perpendicular component of the force due to an electric field becomes

$$F_{E,\perp} = [s_\perp(\beta_E)]\, q\alpha E_\perp = qE_\perp\sqrt{1-\beta_E^2}. \tag{2.56}$$

The resulting force can be approximated (at low speeds β_E) by

$$F_{E,\perp} \cong qE_\perp\left(1-\frac{\beta_E^2}{2}\right). \tag{2.57}$$

However, this expression is not consistent with the force between two current carrying wires. In particular, the scaling of the term β_E^2 has the opposite sign in Eq. (2.57) when compared to the expression in Eq. (2.48). The use of the expression in Eq. (2.57) would lead to a force

$$F_{1,2} = \frac{\mu I_1 I_2}{2\pi r}\hat{r} \tag{2.58}$$

similar to Eq. (2.55); however, the force between two wires that are carrying current in the same direction is repulsive, which is incorrect.

Remark 25 (Comparison of parallel and perpendicular slip impact) *The change is the parallel force between wires carrying current has the opposite sign as the perpendicular force between wires carrying current as seen in Eq. (2.48).*

2.5 Optics

The field velocities (V_E, V_B) introduce extra terms in Maxwell's equations that are removed to retain co-ordinate invariance. It is shown that the proposed relative-velocity (RV) model captures relativistic effects in: (i) the propagation speed of light; (ii) stellar aberration; (iii) the transverse Doppler effect; and (iv) the convection of light by moving media.

2.5.1 Relative-velocity in Maxwell's equations

Consider an electric E and a magnetic M field, which are stationary with respect to an inertial frame O_2, and satisfy Maxwell's equations in free space without charges

$$\nabla \times E = -\frac{\partial B}{\partial t} \tag{2.59}$$

$$\nabla \times B = \epsilon\mu \frac{\partial E}{\partial t}. \tag{2.60}$$

Consider the same equation in a different inertial frame O_1 in which the inertial frame O_2 is moving with constant velocity $V = V_{O2}$ as shown in Fig. 2.1. The Galilean transformation between the two frames

$$X_1 = X_2 + Vt$$

gives the following relations at any location (X_2 in frame O_2 or $X_1 - Vt$ in frame O_1)

$$\text{Frame } O_2 \qquad \text{Frame } O_1 \tag{2.61}$$

$$E(a,b), \quad B(a,b) \qquad E(a,b), \quad B(a,b) \tag{2.62}$$

$$a = X_2, \quad b = t, \qquad a = X_1 - Vt, \quad b = t \tag{2.63}$$

$$V_E = 0, \quad V_B = 0 \qquad V_E = V, \quad V_B = V \tag{2.64}$$

$$\frac{\partial E}{\partial t} = \frac{\partial E}{\partial b} \qquad \frac{\partial E}{\partial t} = \frac{\partial E}{\partial a}(-V_E) + \frac{\partial E}{\partial b} \tag{2.65}$$

$$= -(V_E \cdot \nabla)E + \frac{\partial E}{\partial b} \tag{2.66}$$

$$\frac{\partial E}{\partial X_2} = \frac{\partial E}{\partial a} \qquad \frac{\partial E}{\partial X_1} = \frac{\partial E}{\partial a}. \tag{2.67}$$

Since the spatial gradient is invariant with frame, in Eq. (2.67), the curl — e.g., $\nabla \times B$ on the left hand side of Eq. (2.60) — is also frame invariant. However, the partial time derivative in Eq. (2.66) has an extra term in frame 2. Therefore, the partial derivative with time, such as $\frac{\partial E}{\partial t}$ on the right hand side of Eq. (2.60), has an extra term $-(V_E \cdot \nabla)E$. Hence, adding the term $(V_E \cdot \nabla)E$ to Maxwell's Eq. (2.60) will make it frame invariant under the relative-velocity-dependent approach; the modified equation becomes

$$\nabla \times B = \epsilon\mu \left(\frac{\partial E}{\partial t} + (V_E \cdot \nabla)E \right). \tag{2.68}$$

Noting that

$$\frac{dE}{dt} = \frac{\partial E}{\partial t} + (V_E \cdot \nabla)E \tag{2.69}$$

and using a similar argument to modify Eq. (2.59), we obtain the following inertial-frame invariant form of Maxwell's equations with terms that include the field velocities (V_E, V_B)

$$\nabla \times E = -\frac{dB}{dt} \tag{2.70}$$

$$\nabla \times B = \epsilon\mu\frac{dE}{dt} \tag{2.71}$$

Remark 26 (Invariance with co-ordinate change) *Electric E and magnetic B fields, with field velocities V_E and V_B, respectively, that satisfy Maxwell's equations in one reference frame also satisfy it in another inertial reference frame with a Galilean transformation of the field velocities. In this sense, the modified Maxwell's Eqs. (2.70,2.71) with the total time derivatives are invariant to Galilean transformations between inertial reference frames.*

Note that the main innovation that enables the form invariance (under Galilean transformations) is the association of velocity fields V_E and V_B with electric and magnetic fields E and B, respectively. An electric field E and magnetic field B with field velocities V_{E,O_1} and V_{B,O_1} that satisfy the modified Maxwell's equations with respect to an inertial observer O_1 also satisfy the same form of modified Maxwell's equations with field velocities $V_{E,O_2} = V_{E,O_1} + v$ and $V_{B,O_2} = V_{B,O_1} + v$ with respect to another inertial observer O_2 where v is the velocity of frame 1 with respect to frame 2. Thus, although the values of the field velocities (V_E and V_B) are different in different frames, the relative-velocity (RV) approach results in the same form of the modified Maxwell's equations in different frames.

Remark 27 (Addition of current density) *It is noted that a current density of the form*

$$\mu J = \mu\epsilon\,(\nabla \cdot E)\,V_E \tag{2.72}$$

can be added to the right hand side of Eq. (2.71) but is not needed in the following discussion on optics.

2.5.2 Propagation speed of light

Consider the following two wave equations, which are considered as disturbances on the nominal electrical E and magnetic B fields, each of which has a field velocity

$$V_E = V_B = V = v_z\hat{z},$$

with magnitude v_z in the $\hat{z}$ direction, given by

$$E = e_x \cos(\omega t - kz)\,\hat{x} \tag{2.73}$$

$$B \;=\; b_y \cos(\omega t - kz)\;\hat{y}. \tag{2.74}$$

The terms in the modified Maxwell's Eqs. (2.70,2.71) for the above wave equations are computed below.

$$\nabla \times B \;=\; -\,b_y k \sin(\omega t - kz)\;\;\hat{x} \tag{2.75}$$

$$\nabla \times E \;=\; e_x k \sin(\omega t - kz)\;\;\hat{y} \tag{2.76}$$

$$\frac{dB}{dt} \;=\; [-\omega \;+ kv_z]\, b_y \sin(\omega t - kz)\;\hat{y} \tag{2.77}$$

$$\frac{dE}{dt} \;=\; [-\omega \;+ kv_z]\, e_x \sin(\omega t - kz)\;\hat{x} \tag{2.78}$$

Substituting Eqs. (2.75-2.78) into the modified Maxwell's Eqs. (2.70,2.71) yields

$$e_x k \;=\; -\,[-\omega \;+ kv_z]\, b_y \tag{2.79}$$

$$-\,b_y k \;=\; \epsilon\mu\,[-\omega \;+ kv_z]\, e_x \tag{2.80}$$

By setting $e_x = b_y c$ and $\mu\epsilon = \frac{1}{c^2}$ both the equations reduce to the common expression

$$ck \;=\; (\omega \;- kv_z)\,. \tag{2.81}$$

Note that the wave propagation speed V_{light} is given by ω/k; therefore, the light propagation speed (in the z-direction) is additive, i.e.,

$$V_{light} \;=\; \omega/k \;\;=\; c \;+ v_z. \tag{2.82}$$

Thus, the modified Maxwell's equations allow the nominal velocity of the field V, in which light is generated, to be added to the standard velocity of light when the field is non-moving — this follows directly from the invariance of modified Maxwell's equations.

Remark 28 (Michelson-Morley null result) *The Michelson-Morley experiment is expected to yield the null result with the relative-velocity (RV) approach with the moving fields because the velocity of light is constant in all directions with respect to frame of measurement (in which light is generated).*

2.5.3 Effect of star's velocity on aberration

In a reference frame on earth, the velocity of the earth $V_e = v_e \hat{V}_e$ adds to the velocity of stellar light to generate the aberration effect, see Eq. (2.82), as in the original explanation by Bradley [14]. The angle of the light direction with respect to earth (θ measured perpendicular to earth's motion as shown in Fig. 2.6) is maximum if the star's velocity $V_s = v_s \hat{V}_s$ reduces the nominal light speed to $c - v_s$ (when angle $\theta_s = 0$). Thus, the maximum change in the light direction with respect to earth is 2θ where

$$\tan\theta \;=\; \frac{v_e}{c - v_s}. \tag{2.83}$$

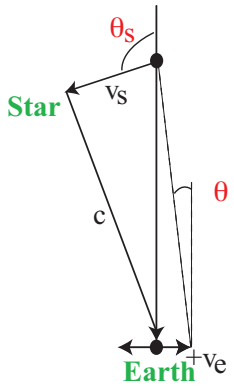

Figure 2.6: Aberration formula based on relative-velocity (RV) matches the classical expression [14].

For small speeds v_s and v_e the above expression is only linear in v_e (and not linear in v_s) — it can be approximated as

$$\theta \approx \frac{v_e}{c}. \tag{2.84}$$

The effect of the star's velocity V_s on the aberration effect (due to Earth's motion) is small if the speed of the star is small, i.e., v_s is much smaller than the nominal velocity of light c. Therefore, with the relative-velocity (RV) approach, stellar aberration appears to be independent of the star's velocity V_s [32] and appears to only depend on the relative change in the observer's velocity [33].

2.5.4 Transverse Doppler effect

Consider the Doppler effect due to addition of velocities in different frames. Let light be generated by a source s moving with velocity $V = v\hat{V}$ relative to the receiver, with angle θ_r with respect to the line between the source and the receiver, measured with respect to the receiver. Light generated by the source has velocity $C_s = c_s\hat{C}_s$ (magnitude $c_s = c$) and angle θ_s. The observed velocity of light is $C_r = c_r\hat{C}_r$ as shown in Fig 2.7.

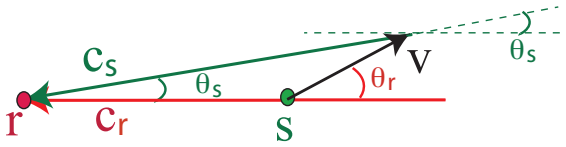

Figure 2.7: Relative-velocity (RV) approach to explain the transverse Doppler effect: Source s, which has relative velocity V with respect to the receiver, generates light whose velocity is $c_s = c$. The observed velocity of the light is at an angle θ_s in the receivers frame/

The magnitude c_r of the observed velocity can be determined using angle θ_r (measured in the receiver frame) as

$$(c_r + v\cos\theta_r)^2 \ + v^2\sin^2\theta_r = c_s^2, \tag{2.85}$$

which implies that

$$c_r \;= -v\cos\theta_r + \sqrt{c_s^2 - v^2\sin^2\theta_r} \;= c\left[-\beta\cos\theta_r + \sqrt{1-\beta^2\sin^2\theta_r}\right] \tag{2.86}$$

where $\beta = v/c$. Hence, the frequencies f_r, f_s in the receiver and source frames, respectively, are related by

$$f_r = f_s\frac{c_r}{c_s} \;= f_s\frac{c_r}{c} \;= f_s\left[-\beta\cos\theta_r + \sqrt{1-\beta^2\sin^2\theta_r}\right]. \tag{2.87}$$

For the transverse case ($\theta_r = \pi/2$),

$$f_r \;=\; \begin{cases} f_s\sqrt{1-\beta^2} & \text{if } \theta_r = \pi/2. \end{cases} \tag{2.88}$$

Note that the relative velocity (RV) expression for transverse Doppler effect in Eq. (2.88) when $\theta_r = \pi/2$ matches the standard relativity (SR) expression

$$f_r = f_s\frac{\left(\sqrt{1-\beta^2}\right)}{(1+\beta\cos\theta_r)} \tag{2.89}$$

$$= f_s\sqrt{1-\beta^2} \quad \text{if } \theta_r = \pi/2. \tag{2.90}$$

2.5.5 Doppler effect under circular motion

Doppler effect between an emitter and absorber in circular motion are similar for both special relativity (SR) and relative velocity (RV) approaches. In particular, the SR-based approach predicts a Doppler effect of [34]

$$f_a = f_e\frac{1-\beta_a\cos(\bar{c},\bar{v}_a)}{1-\beta_e\cos(\bar{c},\bar{v}_e)}\left(\frac{\gamma(\beta_a)}{\gamma(\beta_e)}\right) \tag{2.91}$$

where f_a is the frequency, $\bar{v}_a$ is the velocity with respect to the laboratory frame, β_a is the relative speed $|\bar{v}_a|/c$ and $\gamma(\beta_a) = \frac{1}{\sqrt{1-\beta_a^2}}$ is the time dilation corresponding to the absorber. Similarly, for the emitter, f_e is the frequency, $\bar{v}_e$ is the velocity with respect to the laboratory frame, β_e is the relative speed $|\bar{v}_e|/c$ and $\gamma(\beta_e) = \frac{1}{\sqrt{1-\beta_e^2}}$ is the corresponding time dilation. $\bar{c}$ is the velocity of light from emitter to absorber in the laboratory frame. In contrast, there is no time dilation in the RV based model, which can lead to potential differences between SR and RV.

SR prediction: When the absorber and emitter are in circular motion with constant angular speed ω in the laboratory frame F_L, as in Fig. 2.8, SR predicts no doppler shift between the emitter and the absorber. In particular, with small angular speeds, the SR prediction in Eq. (2.91) becomes

$$f_a = f_e\frac{1-\beta\cos(\theta+\frac{\pi}{2})}{1-\beta\cos(\theta+\frac{\pi}{2})}\left(\frac{\gamma(\beta)}{\gamma(\beta)}\right) \;= f_e, \tag{2.92}$$

where $\beta = \frac{\omega r}{c}$, r is the radius of the circular orbit, and c is the speed of light. This result is independent of the angle θ (in Fig. 2.8 (right)) as long as the emitter and the absorber are at the same distance r from the center of rotation. This lack of Doppler shift has been verified [35] for the case when the emitter and absorber are on opposite sides along the diameter with $\theta = \pi/2$ as in Fig. 2.8 (left).

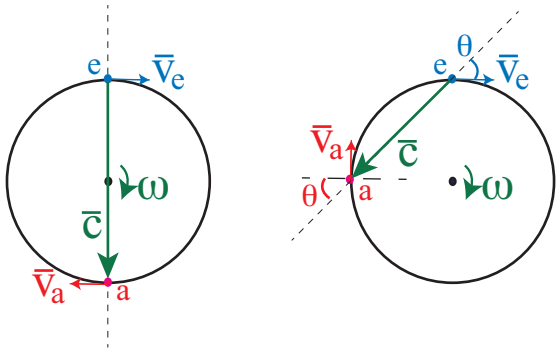

Figure 2.8: Experimental setup with circular motion of absorber and emitter in the laboratory frame F_L

RV prediction: When the absorber and emitter are in circular motion as in Fig. 2.8, RV predictions also matches SR predictions and experimental observations in [35]. For example, as shown in Fig. 2.9, the velocity of light $\overline{c}_e$ from the emitter (in the laboratory frame) is given by

$$\overline{c}_e = \overline{v}_e + \overline{c} \tag{2.93}$$

and the velocity of light $\overline{c}_a$ observed by the absorber (in the absorbers frame) is given by, using Eq. (2.93),

$$\overline{c}_a = \overline{c}_e - \overline{v}_a, \tag{2.94}$$

where the speeds of the absorber and emitter are the same $v_a = v_e = v = \omega r$. Here the path of the light c_e from the emitter to the absorber is approximately along the line connecting the two since the circular motion speeds $v_e = v_a$ are small compared to the speed of light, and the radius r of the circular motion is small. Note that triangles $\triangle efa$ and $\triangle abe$ are similar since they share a common side $\overline{c}_e$, have similar sides $v_a = v_e = v = \omega r$ and the same angle between the similar sides, $\angle fea = \angle bae = \theta + \pi/2$. Therefore, the speed of light c_a observed by the absorber (in the absorbers frame) is the same as the speed of light c observed by the emitter (in the emitters frame), $c_a = c$. Hence, RV predicts no doppler shift between the emitter and the absorber,

$$f_a = f_e \frac{c_a}{c} = f_e. \tag{2.95}$$

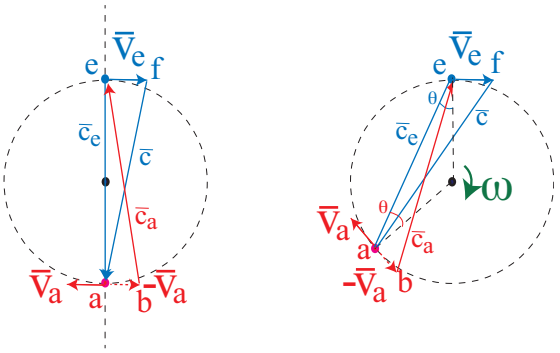

Figure 2.9: Relative velocity (RV) based prediction of light speeds for circular motion of absorber and emitter in the laboratory frame F_L as in Fig. 2.8.

2.5.6 Convection of light in moving media

The effect of moving media on the velocity of light through the media is shown to be similar to Fresnel's drag formula without the need for Lorentz contraction that was developed to explain this effect.

Consider a media moving with relative velocity $V = v\hat{V}$ in frame 1 as shown in Fig. 2.10. For an observer O_1 in frame 1, the speed of light generated in frame 1 is c (in vacuum); the goal is to estimate the effective speed of light c_{eff,O_1} through the moving media for the same observer (in frame 1). The passage of light in the moving media can be differentiated into two types: (a) the passage of light through particles in the media; and (b) passage through vacuum in the media — this approach is adapted from the method by Michelson and Morley [36]. Let the mean length between particles be L and the mean length of each particle be αL — these are measured in frame 2 that is fixed on the moving media (as shown in Fig. 2.10). It is noted that the positive factor α tends to be small, i.e., the particle length is small when compared to the distance between particles [36].

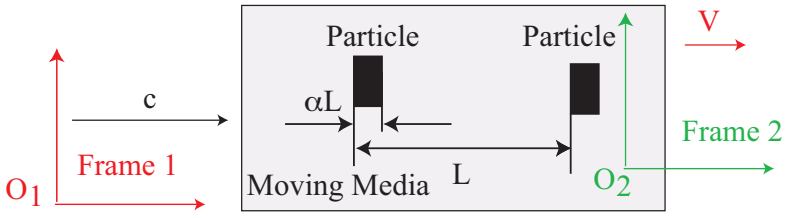

Figure 2.10: Relative-velocity approach to model the convection effect (Fresnel drag) in moving media. In the moving media (frame 2) the mean length between particles is L and the average length of each particle is αL.

Consider an observer O_2 in frame 2; let the nominal speed of light through a particle in the medium be c_m when the relative velocity V is zero. However, due to motion of the media, the speed of light (generated in frame 1) through particle is $c_m - v$ and through vacuum is $c - v$ for observer 2. The total velocity is not a linear summation of the two

velocities; the effective speed of light c_{eff,O_2} through the medium (for a fixed observer in frame O_2) is given by

$$\frac{L}{c_{eff,O_2}} = \frac{\alpha L}{c_m - v} + \frac{(1-\alpha)L}{c - v} \quad \text{i.e.,} \quad c_{eff,O_2} = \frac{1}{\frac{\alpha}{c_m - v} + \frac{(1-\alpha)}{c-v}}. \tag{2.96}$$

The nominal speed C_{nom} of the light through the media with zero relative velocity is obtained by setting $v = 0$ in Eq. (2.96) as

$$c_{nom} = \frac{1}{\frac{\alpha}{c_m} + \frac{(1-\alpha)}{c}}. \tag{2.97}$$

The effective velocity expression in Eq. (2.96) can be expanded in terms of the relative velocity V as (where the higher order terms are neglected)

$$\begin{aligned} c_{eff,O_2} &\approx c_{nom} + \frac{-1}{\left(\frac{\alpha}{c_m} + \frac{(1-\alpha)}{c}\right)^2}\left(\frac{\alpha}{c_m^2} + \frac{(1-\alpha)}{c^2}\right) v \\ &= c_{nom} - \frac{c_{nom}^2}{c^2}\left(\frac{\alpha c^2}{c_m^2} + (1-\alpha)\right) v \\ &= c_{nom} - \frac{1}{\eta^2}\left(\frac{\alpha c^2}{c_m^2} + (1-\alpha)\right) v \end{aligned} \tag{2.98}$$

where η is the media's coefficient of refraction. If α is small, then the expression in Eq. (2.98) can be approximated by

$$c_{eff,O_2} \approx c_{nom} - \frac{1}{\eta^2} v. \tag{2.99}$$

Rewriting in terms of observer O_1 in frame 1, by adding v to the expression, leads to

$$\begin{aligned} c_{eff,O_1} &= c_{eff,O_2} + v = c_{nom} - \frac{1}{\eta^2} v + v \\ &= c_{nom} + \left(1 - \frac{1}{\eta^2}\right) v. \end{aligned} \tag{2.100}$$

Therefore, the RV model predicts that the velocity of light in a media moving with velocity v (with respect to a stationary observer) is seen (by the stationary observer) to increase by, from Eq. (2.100)

$$\left(1 - \frac{1}{\eta^2}\right) v, \tag{2.101}$$

where η is the media's coefficient of refraction. This expression exactly matches the SR prediction of the classical Fresnel drag seen in experiments, e.g., see Equation (44) in [37].

2.6 Chapter conclusions

This chapter presented a relative-velocity (RV) based electromagnetism model, which yields a plausible rationale for variable-speed-of-light cosmology discussed in Chapter 1. The main innovation is the association of velocities with fields wherein the force between the field and a particle depends on the relative velocity between the particle and the field. The interesting aspect of this relative velocity (RV) model is that it matches observations in optics such as Fresnel drag, which (in conjunction with Michelson Morley experiment) was one of the problems that the Lorentz transformation was trying to resolve. Moreover, the proposed RV approach matches electromagnetism effects from CRT data.

3 Testing the relative-velocity model

The previous Chapter 2 developed a relative-velocity-dependent (RV) model that matches standard relativity (SR) observations. In the current chapter, potential differences, in longitudinal Doppler effect is explored to experimentally test and comparatively evaluate the predictions of the RV and SR models.

3.1 Overview of differences in longitudinal Doppler effect

The main idea is that differences in the longitudinal Doppler effect, between the predictions of the relative-velocity-based approach and standard relativity, could be used to match predictions with observations for comparative evaluation. In particular, the relative-velocity-based approach predicts a Doppler effect of (from Eq. 2.87 with $\theta_r = 0$)

$$f_r = f_s\,(1-\beta) \tag{3.1}$$

that does not have a nonlinear effect with respect to (wrt) normalized speed β. In contrast, the relativistic Doppler effect would predict a nonlinear effect wrt normalized speed β, since, from Eq. (2.89) with $\theta_r = 0$,

$$f_r \;= f_s \frac{\left(\sqrt{1-\beta^2}\right)}{(1+\beta)} \;= f_s \frac{\left(\sqrt{1-\beta}\right)}{\left(\sqrt{1+\beta}\right)}, \tag{3.2}$$

A challenge is that the predictions of both theories match exactly at low normalized speeds β. In particular, SR prediction becomes

$$f_r \;\approx f_s(1-\beta) \tag{3.3}$$

for low normalized speeds β from Eq. (3.2), which matches the RV prediction in Eq. (3.1). However, the two predictions will diverge at high normalized speeds β. Therefore, the differences between SR and RV predictions should be noticeable when the normalized speed β is high, e.g., in modern high-energy experiments, which are discussed in this chapter.

3.2 SR predictions of high-energy ion experiments

High energy ion experiments assess time dilation, and can be used to experimentally evaluate the differences between the predictions of the SR and RV theories. In high energy ion experiments, Doppler-shifted lasers are used to excite transitions in high-energy ions, and then, observe the resulting emissions to evaluate time dilation γ. In particular, an ion moving with speed $v = \beta c$ with respect to a laboratory frame F_L can be excited by using parallel (co-propagating) or anti-parallel (counter-propagating) lasers as in Fig. 3.1.

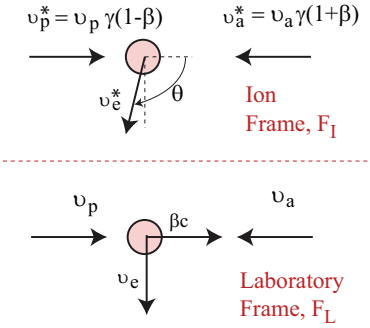

Figure 3.1: Laser frequencies ν_p, ν_a in the laboratory frame F_L are Doppler shifted to frequencies ν_p^*, ν_a^* in a frame F_I that is moving with the ion (circle) at speed $v = \beta c$. Photons emitted at frequency ν_e^* in the ion frame F_I are observed at frequency ν_e in the laboratory frame F_L perpendicular to the moving ions.

The relations between associated laser frequencies ν_p, ν_a (parallel and anti-parallel to the ion velocity with respect to the laboratory frame F_L) and ν_p^*, ν_a^* (parallel and anti-parallel to the ion velocity with respect to a frame F_I attached to the moving ion) are given by SR Doppler expressions as, e.g., [38, 39]

$$\nu_p^* = \nu_p \gamma(1-\beta) \tag{3.4}$$

$$\nu_a^* = \nu_a \gamma(1+\beta) \tag{3.5}$$

and

$$\gamma = 1/\sqrt{1-\beta^2} \tag{3.6}$$

is the time dilation. Similarly, the emission frequency ν_e^* of photons from the ions (with respect to the ion frame F_I) and the detection frequency ν_e perpendicular to the moving ions with respect to the laboratory frame F_L, as shown in Fig. 3.1, are related by (from Eq. (2.89) with angle $\theta_r = \pi/2$)

$$\nu_e \;= \nu_e^* \left(\sqrt{1-\beta^2}\right) \;= \frac{1}{\gamma}\nu_e^* \tag{3.7}$$

3.2.1 Evaluating Potential Lorentz Violation

The ratio R , given by

$$R = \frac{\nu_p \nu_a}{\nu_p^* \nu_a^*} \;= \frac{1}{\gamma^2(1-\beta^2)} \;= 1, \tag{3.8}$$

is independent of the speed of the ions. Potential dependence of the measured ratio R on speed β is used to evaluate time dilation predicted by SR and thereby, to evaluate potential Lorentz violation.

The frequency terms ν_p^*, ν_a^* needed to evaluate the expression for R (in Eq. 3.8) are not directly measurable. This inability to measure ν_p^*, ν_a^* can be avoided if the lasers excite a known transition, say at frequency ν_e^* in the ion frame F_I. For example, in saturation spectroscopy [38, 40], one of the laser frequencies is kept constant and the other frequency is varied to observe the Lamb dip in the fluorescence spectrum, which indicates that both lasers are acting on ions with the same speed, i.e.,

$$\nu_p^* = \nu_e^* \quad \text{and} \quad \nu_a^* = \nu_e^*. \tag{3.9}$$

Then, the ratio R (in Eq. 3.8) can be rewritten as

$$R \;= \frac{\nu_p \nu_a}{(\nu_e^*)^2} \;= \frac{\nu_p \nu_a}{\nu_p^* \nu_a^*} \;= \frac{1}{\gamma^2(1-\beta^2)} \;= 1. \tag{3.10}$$

Remark 29 *Since the experiments rely on the Lamb dip in the fluorescence spectrum to ensure that both lasers are acting on ions with the same speed, the results of the experiment can depend on which emission frequencies are being observed in the laboratory frame.*

3.2.2 Transition Frequency Shift

Ideally, the transition frequency ν_e^* in the moving ion frame F_I should be the same as the transition frequency ν_o for ions that are stationary in the laboratory frame F_L, and is therefore known — the transition frequency ν_o can be determined with high accuracy using stationary ions in the laboratory frame F_L. However, the transition frequency for the moving ions can get shifted (i.e., $\nu_e^* \neq \nu_o$) due to external fields and charged particles causing Stark and Zeeman effects, e.g., [40].

The potential shift in the transition frequency implies that the transition frequency ν_e^* excited in the moving ion cannot be assumed to be exactly the same as the transition frequency ν_o measured for stationary ions under different experimental conditions. Moreover, this shifted frequency ν_e^* is not directly measurable (in the moving ion frame F_I) — although the transition frequency ν_o of the stationary ions (in laboratory frame F_L) is known. Therefore, the ratio R (in Eq. 3.10) cannot be evaluated directly from the measurements, and an expression in terms of the directly measurable frequencies (ν_a, ν_p, ν_o) is sought.

3.2.3 Effect of PMT Pre-Filters

Measurements of the number of photons emitted by the moving ions (to determine excitation of the ion transition) by the photomultiplier tubes (PMTs) will not be independent of photon frequency if optical pre-filters are used before the PMTs. For example, let the emission be observed using an interference filter (before the PMT) centered at

$$\nu_e = \alpha \nu_o \tag{3.11}$$

with respect to the laboratory frame F_L (where the ν_o is the transition frequency of stationary ions) to detect the laser frequency where the Lamb dip occurs. In this case, the observed Lamb dip corresponds to emitted photons of frequency ν_e^* in the ion frame F_I by (from Eq. 3.7)

$$\nu_e^* \ = \gamma\nu_e \ = \gamma\alpha\nu_o. \tag{3.12}$$

Remark 30 *The frequency ν_e of emission in the laboratory frame is expected to be smaller than the frequency ν_e^* of emission in the ion frame from Eq. (3.16), when photons arrives perpendicular to the laser axis (i.e., deviation angle $\phi = 0$). However, the centerline of the prefilter is chosen for a larger emission frequency ν_e with wavelength $\lambda_{PMT} = 500nm$ in the laboratory frame when compared to the stationary emission frequency ν_e^* with wavelength $\lambda_o = 548.5nm$ in the ion frame [40], resulting in $\alpha = 1.097 > 1$. Thus, the constant $\alpha > 1$ in current high-speed ion experiments.*

The theoretical expression R_o that can be evaluated in terms of measurable frequencies ν_o, ν_p, ν_a (in the laboratory frame F_L) can be found from Eqs. (3.9, 3.10, 3.12) as

$$R_o \ = \frac{\nu_p\nu_a}{(\nu_o)^2} \ = \frac{\gamma^2\alpha^2\nu_p\nu_a}{(\nu_e^*)^2} \ = \gamma^2\alpha^2\frac{\nu_p\nu_a}{\nu_p^*\nu_a^*} \ = \gamma^2\alpha^2\frac{\nu_p\nu_a}{\nu_a\gamma(1+\beta)\nu_p\gamma(1-\beta)} \ = \frac{\alpha^2}{1-\beta^2} > 1. \tag{3.13}$$

Remark 31 *With $\alpha > 1$ (in current experiments) and $1 - \beta^2 < 1$, the expected value of R_o in Eq. (3.13) is necessarily greater than one, if the measured emissions are perpendicular to ion motion in the laboratory frame.*

3.3 Experimental observations do not match SR predictions

Experimental observations find this ratio $R_{o,exp}$ of the product of the laser frequencies $\nu_{p,exp}$ $\nu_{a,exp}$ to the transition frequency $\nu_{o,exp}$ of the stationary ion to be a constant

$$R_{o,exp} \ = \frac{\nu_{p,exp} \ \ \nu_{a,exp}}{(\nu_{o,exp})^2} \ = 1 \tag{3.14}$$

that is independent of the speed β [40] where the subscript *exp* indicates an experimentally obtained value. This results in a difference between theoretical (R_o) and experimental ($R_{o,exp}$) predictions of this ratio (from Eqs. 3.13, 3.14) when $\alpha = 1$,

$$R_o \neq R_{o,exp}. \tag{3.15}$$

Remark 32 *For the high speed experiments with ion speed $\beta = 0.338$ [40], with $\alpha = 1.096$,*

$$R_o = 1.3561$$

from Eq. (3.13) by considering the Doppler effects, which is much different from $R_o = 1$ reported when Doppler effects are neglected.

Thus, experimental results do not match theoretical predictions when Doppler effects are not neglected.

3.4 Potential impact of emission angle

A potential explanation is that the measured emissions are independent of the PMT prefilters, and that the measured photons can be assumed to directly correspond to emissions at $\lambda_e^* = \lambda_o = 548.5nm$ perpendicular to the motion of the ions, in the ion frame (where λ_o is measured for stationary ions) [43]. However, this leads to a substantially large angles (upto 20^o) in the laboratory frame, which would imply that the experiment does not sufficiently focus on emissions at a specific angle-frequency relationship — and the measurements cannot be sure of the frequency of the emissions — especially, in the presence of large Doppler effects with ion speeds as high as $\beta = 0.338$ [40].

From special relativity (SR), the transverse Doppler provides a unique relation between the ratio of the emitted photon frequencies ν_e^* (in the ion frame F_I), ν_e (in the laboratory frame F_L), and the measurement angle ϕ (as in Fig. 3.2)

$$R_\nu = \frac{\nu_e^*}{\nu_e} = \frac{\lambda_e}{\lambda_e^*} = \frac{[1 - \beta \sin\phi]}{\sqrt{1-\beta^2}} = \gamma\,[1 - \beta \sin\phi] \tag{3.16}$$

where the measurement angle ϕ is the deviation of the photomultiplier tube (PMT) axis from the perpendicular to the laser axis (and the ion velocity) in the laboratory frame F_L, λ_e^*, λ_e are the corresponding wavelengths, $v = \beta c$ is the speed of the ion, and c is the speed of light.

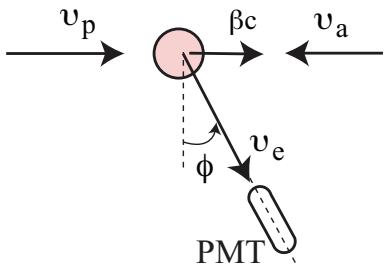

Figure 3.2: Experimental setup in the laboratory frame F_L

If the photon emissions are at $\lambda_e^* = \lambda_o = 548.5nm$ in the ion frame (where λ_o is measured for stationary ions), then the expected wavelength λ_e (in the laboratory frame) at a measurement angle ϕ is shown in Fig. 3.3 for two experimental cases: (i) $\beta = 0.064$ [41]; and (ii) a higher speed $\beta = 0.338$ [40]. However, the measurement angle of $\phi = 0$ of the PMT axis in previous experiments, e.g., [40, 41], does not match the center of the filters used before the PMT. The center $\lambda_{PMT} = 548nm$ of the interference filter used before the PMT (Ref. [41], page 42) for $\beta = 0.064$ matches the expected ion emissions ($\lambda_o = 548.5nm$ in the ion frame) when the PMT axis is $\phi = 3$ degrees away from the perpendicular to the ion velocity (see Fig. 3.3). This deviation from the perpendicular becomes even more significant at higher ion speeds. For example, with $\beta = 0.338$ [40], the center of the BG39 filter is at $\lambda_{PMT} = 500nm$, which would match emissions from the expected transition at λ_o when the angle of the PMT axis is $\phi = 25$ degrees. While the

centerline of the interference filter $\lambda_{PMT} = 548nm$ is close to the expected wavelength of $\lambda_e = 549.6nm$ when the photon arrives perpendicular to the laser axis (i.e., deviation angle $\phi = 0$) with $\beta = 0.064$, the centerline at $\lambda_{PMT} = 500nm$ is substantially further away from $\lambda_e = 582.8nm$ for the $\beta = 0.338$ case with deviation angle $\phi = 0$.

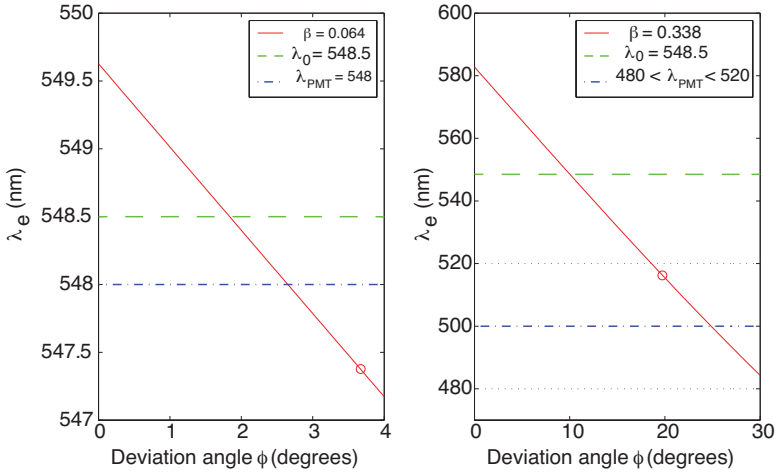

Figure 3.3: Variation of expected emission wavelength λ_e in the laboratory frame F_L for different measurement angles ϕ.

Even if the majority of the photons are assumed to be perpendicular to the laser axis in the ion's frame of reference (rather than perpendicular in the laboratory frame), the SR expression for the measured emissions in the laboratory frame,

$$\lambda_e = \lambda_e^*/\gamma = \lambda_o/\gamma; \qquad \cos(\pi/2 - \phi) = \beta \tag{3.17}$$

yields $\lambda_e = 547.3nm, \phi = 3.7$ degrees (for $\beta = 0.064$) and $\lambda_e = 516nm, \phi = 19.8$ degrees (for $\beta = 0.338$) represented by circles in Fig. 3.3. Thus, a noticeable deviation ϕ from the perpendicular to the laser axis (in the laboratory frame) is expected when compared to the perpendicular placement of the PMT axis ($\phi = 0$) in the experiments [40, 41].

The loss of control over the angle ϕ of the photons entering the PMT, coupled with the relatively broad half-width of the filter, implies that the experiment cannot ensure that the photon being measured has the expected wavelength-angle (λ_e, ϕ) relation. Then, the experimental analysis (e.g., for the two-level system in [41]) needs to rely on the assumption that the measured photon is from a transition that was excited at $\nu_o = c/\lambda_o$ in the ion's frame of reference under the specific experimental conditions. However, the results cannot validate SR and rule out Lorentz violation without this assumption that the transition being excited still corresponds to ν_o in the ion's frame (under the experimental conditions). As discussed earlier, photons at frequency ν_o (the center of the filter with $\beta = 0.064$ in the laboratory frame) that are aligned with the PMT axis ($\phi = 0$) would be observed by the PMT, which can imply Lorentz violation.

3.4.1 Other Effects

It is possible that other effects (such as variations in the observation angle) might explain or reduce the apparent Lorentz violation; further work is needed to investigate such effects. For example, previous work has shown that resonance fluorescence can be affected by the observational angle [42]. Therefore, the experimental results would be affected if the PMT is not measuring emissions that are exactly perpendicular to the ion beam. Further analysis would be needed to evaluate such angle-deviation effects.

It is noted that systematic SR violation (or Lorentz violation) is directly related to the amount of uncertainty in the transition. Uncertainty can occur because in addition to potential changes in the transition under the experimental conditions, the transition itself is a distribution, with a range of values. Self-selection (of the transition) is possible depending on the conditions under which the photons are observed in the Laser Spectroscopy experiment, since the approach depends on evaluating variations in intensity of the emissions. Filters used to select the photons being measured should be tuned to the right frequency for the observation angle. If the filters are too broad the approach cannot rule out Lorentz violation. For example, let the Lorentz violation modify the time dilation from γ to $\gamma\Delta_\gamma$, and let the self-selected transition be $\nu_o\Delta_{\nu_o}$ instead of ν_o, under the specific experimental conditions. Then, SR analysis, which assumes no change in the transition (for a two-level transition [41]), yields

$$\nu_p = \frac{\nu_o}{\gamma(1-\beta)}; \qquad \nu_a = \frac{\nu_o}{\gamma(1+\beta)}, \tag{3.18}$$

where ν_p and ν_a are the measured frequencies (in the laboratory frame) of the lasers parallel and anti-parallel to the ion velocity. However, potential Lorentz violation, which matches the experimentally observed laser frequencies (ν_p, ν_a), can be found as

$$\nu_p = \frac{\nu_o}{\gamma(1-\beta)} = \frac{\nu_o\Delta_{\nu_o}}{\gamma\Delta_\gamma(1-\beta)} \tag{3.19}$$

$$\nu_a = \frac{\nu_o}{\gamma(1+\beta)} = \frac{\nu_o\Delta_{\nu_o}}{\gamma\Delta_\gamma(1+\beta)}. \tag{3.20}$$

Note that the Lorentz violation factor has the potential to be of the same order as the change in the transition frequency with

$$\Delta_\gamma = \Delta_{\nu_o}. \tag{3.21}$$

Although, bounds on the potential deviation in the transition $(\Delta_{\nu_o} - 1)$ can be estimated theoretically, an experimental design that accounts for the transverse Doppler effect, enables validation of the assumption that the transition being evaluated in the moving ion (under the experimental conditions) is the same as the expected transition ν_o (measured for stationary ions).

3.5 RV prediction matches current observations

RV predictions also match current observations with the use of a prefilter $\nu_e = \alpha\nu_o$ as in Eq. (3.11) and with the assumption that the measured photons can have a nonzero deviation angle $\phi \neq 0$ as in Fig. 3.4 and assumed in current SR-based experimental analysis that does not account for the substantial Doppler shift.

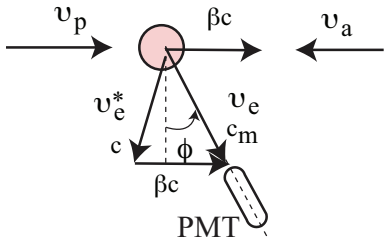

Figure 3.4: RV-based analysis. Light at speed c and frequency $\nu_e^* = \nu_o\sqrt{1-\beta^2}$ in the ion frame is observed at speed c_m and frequency $\nu_e = \alpha\nu_o$ in the laboratory frame. The speed of the ion is βc.

In particular, the associated emissions can be at frequency $\nu_e^* = \nu_o\sqrt{1-\beta^2}$ for the emissions in the ion frame with RV models. As a result, the angle ϕ of the emissions in the laboratory frame is given by

$$\frac{c_m}{c} = \frac{\nu_e}{\nu_e^*} = \frac{\alpha}{\sqrt{1-\beta^2}} \tag{3.22}$$

$$c^2 = c_m^2 + (\beta c)^2 - 2c_m(\beta c)\sin(\phi) \tag{3.23}$$

$$\sin(\phi) = \frac{c_m^2 + (\beta c)^2 - c^2}{2c_m\beta c} = \frac{(\frac{\alpha}{\sqrt{1-\beta^2}})^2 + \beta^2 - 1}{2(\frac{\alpha}{\sqrt{1-\beta^2}})\beta} \tag{3.24}$$

resulting in

$$\nu_e^* = \frac{\sqrt{1-\beta^2}}{\alpha}\nu_e = \frac{\sqrt{1-\beta^2}}{\alpha}(\alpha\nu_o) = \nu_o\sqrt{1-\beta^2} = \nu_p^* = \nu_a^* \tag{3.25}$$

with $\phi = 36.8^o$ for $\beta = 0.338$ and $\alpha = 1.096$.

Moreover, the relationship between laser frequencies ν_p, ν_a (parallel and anti-parallel to the ion velocity with respect to the laboratory frame F_L) and ν_p^*, ν_a^* (parallel and anti-parallel to the ion velocity with respect to a frame F_I attached to the moving ion) are given using relative-velocity-based approach using Eq. (2.87) as

$$\nu_p^* = \nu_p(1-\beta) = \nu_o\sqrt{1-\beta^2} \tag{3.26}$$

$$\nu_a^* = \nu_a(1+\beta) = \nu_o\sqrt{1-\beta^2}. \tag{3.27}$$

Then, the product of the laser frequencies divided by ν_o^2 would lead to,

$$R_{RV} = \frac{\nu_p\nu_a}{\nu_o^2} = \frac{\frac{\nu_o\sqrt{1-\beta^2}}{(1-\beta)}\frac{\nu_o\sqrt{1-\beta^2}}{(1+\beta)}}{\nu_o^2} = 1. \tag{3.28}$$

Thus, RV can also predict the observed relationship between the laser frequencies nu_p, ν_a and the emission frequency ν_o for stationary ions, if the measurements do not restrict the frequency-angle relationship of the emissions in the laboratory frame.

3.6 Future experimental differentiation between SR and RV

To enable experimental testing of RV and SR, future experimental design could verify the frequency of the measured photons in the laboratory frame and thereby account for the substantial Doppler shift in the emissions. For example, it might be possible (a) to place filters before the PMT, centered at the frequency $\nu_e = \nu_o/\gamma$ (esp for large β such as 0.338), and (b) to facilitate collimation to ensure that measured photons measured correspond to angle $\phi = 0$ in the laboratory frame as in Fig. 3.2. This would guarantee that there is no shift in the transition frequency in the ion frame F_I, i.e., emissions measured correspond to frequency ν_o in the ion frame, which is the known value for stationary ions.

3.6.1 SR prediction

With the use of a prefilter

$$\nu_e = \frac{\nu_o}{\gamma} \tag{3.29}$$

and collimation to ensure measurement of photons with angle

$$\phi = 0 \tag{3.30}$$

in the laboratory frame, SR would predict that the frequency ν_e^* of the emissions in the ion frame is given by (from Eq. (3.16) with $\phi = 0$)

$$\nu_e^* = \gamma\nu_e = \gamma\frac{\nu_o}{\gamma} = \nu_o. \tag{3.31}$$

Then, the product of the laser frequencies divided by ν_o^2 would lead to, from Eqs. (3.4, 3.5) similar to Eq. (3.8) ,

$$R_{SR} = \frac{\nu_p\nu_a}{\nu_o^2} = \frac{\frac{\nu_p^*}{\gamma(1-\beta)}\frac{\nu_a^*}{\gamma(1+\beta)}}{\nu_o^2} = \frac{\frac{\nu_o}{\gamma(1-\beta)}\frac{\nu_o}{\gamma(1+\beta)}}{\nu_o^2} = \frac{1}{\gamma^2(1-\beta^2)} = 1. \tag{3.32}$$

3.6.2 RV prediction

With the use of a prefilter $\nu_e = \frac{\nu_o}{\gamma}$ as in Eq. (3.29) and and collimation to ensure measurement of photons with angle $\phi = 0$ as in Eq. (3.30) in the laboratory frame,

RV would predict that a frequency ν_e^* of the emissions in the ion frame given by (from Eq. (2.88) with $\nu_e = f_r, \nu_e^* = f_s$)

$$\nu_e = \nu_e^* \sqrt{1-\beta^2} = \frac{\nu_e^*}{\gamma} = \frac{\nu_o}{\gamma}. \tag{3.33}$$

resulting in (same as SR prediction)

$$\nu_e^* = \nu_o. \tag{3.34}$$

Thus, for this case, RV predicts the same emission frequency ν_o (a known value) in the ion frame as with SR. The relationship between laser frequencies ν_p, ν_a (parallel and anti-parallel to the ion velocity with respect to the laboratory frame F_L) and ν_p^*, ν_a^* (parallel and anti-parallel to the ion velocity with respect to a frame F_I attached to the moving ion) are given using relative-velocity-based approach using Eq. (2.87) as

$$\nu_p^* = \nu_p(1-\beta) \tag{3.35}$$

$$\nu_a^* = \nu_a(1+\beta). \tag{3.36}$$

Then, the product of the laser frequencies divided by ν_o^2 would lead to,

$$R_{RV} = \frac{\nu_p \nu_a}{\nu_o^2} = \frac{\frac{\nu_p^*}{(1-\beta)}\frac{\nu_a^*}{(1+\beta)}}{\nu_o^2} = \frac{\frac{\nu_o}{(1-\beta)}\frac{\nu_o}{(1+\beta)}}{\nu_o^2} = \frac{1}{(1-\beta^2)}. \tag{3.37}$$

3.7 Chapter conclusions

The transverse Doppler effect, in the emissions, is substantial in high-energy ion experiments [43]. It should be accounted for in order to rule out Lorentz violations in high-energy ions and validate SR, and rule out RV-based models.

Early experiments, with much smaller ion speeds, had relatively-small angle deviations due to transverse Doppler. For example, with $\beta = 0.004$ [44], the angle deviation was only $\phi = 0.2$ degrees. Therefore, it was difficult to experimentally verify the transition frequency being excited in the moving ion. However, with larger speeds ($\beta = 0.064$ and $\beta = 0.338$), the need to assume that the transition being excited is still ν_o in the moving ion frame, can be removed by including the transverse Doppler effect in the experimental measurements, i.e., matching the PMT axis angle ϕ to the center ν_e of the PMT filter according to the (ν_e, ϕ) relation in Eq. (3.16) (with $\nu_e^* = \nu_o$). Additionally, deviations of measured photons from this (ν_e, ϕ) relation should be minimized, in high energy experiments, by: (i) using collimation to limit the variation from the chosen angle ϕ; and (ii) selecting narrow filters (e.g., when compared to BG39 at $\beta = 0.338$ [40]) centered around the chosen frequency ν_e. Such experimental efforts could clarify and quantify, better, the potential Lorentz violation identified in this chapter and its potential effect on systematic errors reported in other related experiments, e.g., when the ions are moving perpendicular to the lasers [44].

Moreover, there is a clear difference between SR and VR predictions with high-energy ion experiments as reflected in Eqs. (3.32) and (3.37). However, current experiments do not sufficiently account for the large Doppler effects, especially, with high ion speeds such as $\beta \approx 0.3$, and have to assume that the emissions are from a specific frequency ν_o in the ion's frame. Selecting appropriate PMT prefilters (to account for the substantial angle-dependent Doppler effect) can lead to isolation of emissions at a specific frequency, and and reduce potential errors in the analysis. Such refinement of the experiments can be used to validate/refute SR and RV predictions. In any case, accounting for the significant Doppler effect is needed to get better estimates of potential Lorentz violation within the SR framework.

4 Bibliography

[1] Ming-Hui Shao. The energy loss of photons and cosmological redshift. *Physics Essays*, 26(2):183–190, June 2013.

[2] Dimitrios Laskaroudis. Spectral redshift does not imply an accelerating expansion of the universe. *Physics Essays*, 26(3):452–456, Sept. 2013.

[3] Walter Petry. Modified Hubble law. *Physics Essays*, 26(2):315–320, June 2013.

[4] Lorenzo Zaninetti. New formulas for the Hubble constant in a Euclidean static universe. *Physics Essays*, 23(2):298–305, June 2010.

[5] Robert B. Driscoll. The Hubble-Humason effect and general relativity need no cosmological expansion. *Physics Essays*, 23(4):584–587, Dec. 2010.

[6] M. R. S. Hawkins. On time dilation in quasar light curves. *Monthly Notices of the Royal Astronomical Society*, 405:1940–1946, 2010.

[7] S. Blondin, T. M. Davis, K. Krisciunas, B. P. Schmidt, J. Sollerman, W. M. Wood-Vasey, A. C. Becker, P. Challis, A. Clocchiatti, G. Damke, A. V. Filippenko, R. J. Foley, P. M. Garnavich, S. W. Jha, R. P. Kirshner, B. Leibundgut, W. Li, T. Matheson, G. Miknaitis, G. Narayan, G. Pignata, A. Rest, A. G. Riess, J. M. Silverman, R. C. Smith, J. Spyromilio, M. Stritzinger, C. W. Stubbs, N. B. Suntzeff, B. E. Tonry, J. L. andTucker, and A. Zenteno. Time dilation in type Ia supernova spectra at high redshift. *The Astrophysical Journal*, 682(2):724–736, September 15 2008.

[8] M. Lopez-Corredoira and C. M. Gutierrez. First tentative detection of anisotropy in the QSO distribution around nearby edge-on spiral galaxies. *Astronomy and Astrophysics*, 461(1):393–404, January 2007.

[9] Halton C. Arp. *Quasars, Redshifts and Controversies*. Cambridge University Press, Cambridge, U.K., 1987.

[10] Adam G. Riess, Alexei V. Filippenko, Weidong Li, and Brian P. Schmidt. Is there an indication of evolution of type IA supernovae from their rise times? *The Astronomical Journal*, 118(6):2668–2674, December 1999.

[11] Mario Livio and J. E. Pringle. On identifying the progenitors of Type Ia supernovae. *Astrophysical Journal Letters*, 740(1), Article number L18:1–4, October 10 2011.

[12] M. H. Cohen, K. I. Kellermann, D. B. Shaffer, R. P. Linfield, A. T. Moffet, J. D. Romney, G. A. Seielstad, I.I.K. Paulinytoth, E. Preuss, A. Witzel, R. T. Schilizzi, and B.J. Geldzahler. Radio-sources with superluminal velocities. *Nature*, 268(5619):405–409, 1977.

[13] Alberto A. Martinez. Ritz, einstein, and the emission hypothesis. *Physics in Perspective*, 6(1):4–28, 2004.

[14] James Bradley. A Letter from the Reverend Mr. James Bradley Savilian Professor of Astronomy at Oxford, and F.R.S. to Dr. Edmond Halley Astronom. Reg., & c. Giving an Account of a New Discovered Motion of the Fix'd. Stars. *Philosophical Transactions*, 35:637–661, 1727.

[15] Jean-Pierre Petit. Cosmological Model with Variable Light Velocity: The interpretation of red shifts. *Modern Physics Letters A*, 3(18):1733–1744, February 15 1988.

[16] S. Devasia. Nonlinear models for relativity effects in electromagnetism. *Zeitschrift fur Naturforschung A*, 64a(5-6):327–340, May-June 2009.

[17] A. R. Thatcher. Newtonian cosmology and Friedmann's equation. *European Journal of Physics*, 3:202–205, 1982.

[18] E. Hubble. Effects of red shifts on the distribution of nebulae. *Astrophysical Journal*, 84:517–554, 1936.

[19] Thomas A. Duffey, Jason E. Pepin, Amy N. Robertson, Michael L. Steinzig, and Kimberly Coleman. Vibrations of complete spherical shells with imperfections. *Journal of Vibration and Acoustics*, 129(3):363–370, 2007.

[20] V. Icke, A. Frank, and A Heske. Weak chaos in long-period variables. *Astronomy and Astrophysics*, 258(2):341–356, 1992.

[21] Eric C. Pearce, Stirling A. Colgate, and Albert G. Petschek. Concerning the high photospheric velocity of the Type 1a supernova 1984a near maximum light. *The Astrophysical Journal*, 325:L33–L34, February 15 1988.

[22] M. Kowalski, D. Rubin, G. Aldering, R. J. Agostinho, A. Amadon, R. Amanullah, C. Balland, K. Barbary, G. Blanc, P. J. Challis, A. Conley, N. V. Connolly, R. Covarrubias, K. S. Dawson, S. E. Deustua, R. Ellis, S. Fabbro, V. Fadeyev, X. Fan, B. Farris, G. Folatelli, B. L. Frye, G. Garavini, E. L. Gates, L. Germany, G. Goldhaber, B. Goldman, A. Goobar, D. E. Groom, J. Haissinski, D. Hardin, I. Hook, S. Kent, A. G. Kim, R. A. Knop, C. Lidman, E. V. Linder, J. Mendez, J. Meyers, G. J. Miller, M. Moniez, A. M. Mourão, H. Newberg, S. Nobili, P. E. Nugent, R. Pain, O. Perdereau, S. Perlmutter, M. M. Phillips, V. Prasad, R. Quimby, N. Regnault, J. Rich, E. P. Rubenstein, P. Ruiz-Lapuente, F. D. Santos, B. E. Schaefer, R. A. Schommer, R. C. Smith, A. M. Soderberg, A. L. Spadafora, L.-G. Strolger, M. Strovink, N. B. Suntzeff, N. Suzuki, R. C. Thomas, N. A. Walton, L. Wang,

W. M. Wood-Vasey, and J. L. Yun. Improved cosmological constraints from new, old and combined supernova datasets. *The Astrophysical Journal*, 686(2):749–778, 2008.

[23] Kevin Heng, Richard McCray, Svetozar A. Zhekov, Peter M. Challis, Roger A. Chevalier, Arlin P. S. Crotts, Claes Fransson, Peter Garnavich, Robert P. Kirshner, Stephen S. Lawrence, Peter Lundqvist, Nino Panagia, C. S. J. Pun, Nathan Smith, Jesper Sollerman, and Lifan Wang. Evolution of the reverse shock emission from SNR 1987A. *The Astrophysical Journal*, 644:959–970, June 20 2006.

[24] A. Kashlinsky, F. Atrio-Barandela, D. Kocevski, and H. Ebeling. A measurement of large-scale peculiar velocities of clusters of galaxies: Results and cosmological implications. *The Astrophysical Journal*, 686:L49–L52, October, 2008.

[25] M.L. McClure and C.C. Dyer. Anisotropy in the Hubble constant as observed in the HST extragalactic distance scale key project results. *New Astronomy*, 12(7):533–543, Oct 2007.

[26] M. Tegmark, A. de Oliveira-Costa, and A.J.S. Hamilton. High resolution foreground cleaned CMB map from WMAP. *Physical Review D*, 68(12), Article Number 123523:724–736, September 15 2003.

[27] C. L. Bennett, R. S. Hill, G. Hinshaw, D. Larson, K. M. Smith, J. Dunkley, B. Gold, M. Halpern, N. Jarosik, A. Kogut, E. Komatsu, M. Limon, S. S. Meyer, M. R. Nolta, N. Odegard, L. Page, D. N. Spergel, G. S. Tucker, J. L. Weiland, E. Wollack, and E. L. Wright. Seven-year wilkinson microwave anisotropy probe (WMAP) observations: Are there cosmic microwave background anomalies? *Astrophysical Journal Supplement Series*, 192(2):1–19, Feb 2011.

[28] A. K. T. Assis. *Weber's Electrodynamics*. Kluwer Academic Publishers, Dordrecht, 1994.

[29] A. K. T. Assis and H. T. Silva. Comparison between Weber's electrodynamics and classical electrodynamics. *Pramana — Journal of Physics*, 55(3):393–404, September 2000.

[30] William Bertozzi. Speed and kinetic energy of relativistic electrons. *American Journal of Physics*, 32:551–555, 1964.

[31] J. J. Thomson. Cathode rays. *The London, Edinburgh, and Dublin Philosophical Magazine and Journal of Science, Fifth Series*, 44(269), October 1897 (*reprinted in Classical Scientific Papers, Physics, by American Elsevier Publishing Company, Inc., New York, 1964, pp. 77-100*).

[32] Kenneth Brecher. Is the speed of light independent of the velocity of the source? *Physical Review Letters*, 39(17):1051–1054, 24 October 1977.

[33] Thomas R. Phipps, Jr. Relativity and aberration. *American Journal of Physics*, 57(6):549–551, June 1989.

[34] C. Moller. *The Theory of Relativity, 2nd Edition.* Clarendon Press, Oxford, 1972.

[35] D C Champeney and P B Moon. Absence of doppler shift for gamma ray source and detector on same circular orbit. *Proceedings of the Physical Society*, 77(2):350–352, feb 1961.

[36] A. A. Michelson and E. W. Morley. Influence of motion of the medium on the velocity of light. *American Journal of Science*, 31(185):377–386, May 1886.

[37] Max Born. *Einstein's Theory of Relativity.* Dover Publication, Inc., New York, revised edition, 1962.

[38] G. Saathoff, S. Karpuk, U. Eisenbarth, G. Huber, S. Krohn, R. M. Horta, S. Reinhardt, D. Schwalm, A.Wolf, and G. Gwinner. Improved test of time dilation in special relativity. *Physical Review Letters*, 91(19):1–4, #190403, November 7 2003.

[39] M. Mansuripur. Doppler shift, stellar abberation, and convection of light by moving media. *Optics and Photonics News*, pages 52–56, April 2003.

[40] C. Novotny, G. Huber, S. Karpuk, and S. Reinhardt et. al. Sub-Doppler laser spectroscopy on relativistic beams and tests of Lorentz invariance. *Physical Review A*, 80:1–5, # 022107, 2009.

[41] Sascha Benjamin Reinhardt. *Measurement of Time Dilation by Laser Spectroscopy on Fast Stored Lithium Ions.* PhD dissertation, Ruperto-Carola University of Heidelberg, Germany, Natural Sciences, November 2005.

[42] De-Zhong Wang and Jin-Yue Gao. Effect of Doppler broadening on resonance fluorescence. *Physics Letters A*, 228:25–28, March 31 1997.

[43] G. Saathoff et. al. Comment on: Lorentz violation in high-energy ions by santosh devasia. *The European Physical Journal C*, 71:1596, 2010.

[44] M. Kaivola, O. Poulsen, E. Riis, and S. A. Lee. Measurement of the relativistic Doppler shift in Neon. *Physical Review Letters*, 54(4):255–258, January, 1985.